Review | Open Access

Chemical Synthesis

Guddati *et al. Chem. Synth.* **2026**, *6*, 63 **DOI:**10.20517/cs.2026.03

Recent developments in electro/photo chemical reduction of CO_2 by ligand-protected Cu nanoclusters with precise crystal structures

Vamsi Guddati[1], Nagasatish Arasala[1], Sachil Sharma[1,*], Gao Li[2,*]

Keywords:
CO_2 adsorption, ECO_2RR/PCO_2RR, ligand-protected Cu metal nanocluster, structure-efficiency relationship, clean and sustainable energy

Citation: Guddati, V.; Arasala, N.; Sharma, S.; Li, G. Recent developments in electro/photo chemical reduction of CO_2 by ligand-protected Cu nanoclusters with precise crystal structures. *Chem. Synth.* **2026**, *6*, 63. https://dx.doi.org/10.20517/cs.2026.03

Received: 4 Jan 2026
First Decision: 26 Jan 2026
Revised: 27 May 2026
Accepted: 29 May 2026
Published: 30 Jul 2026

Academic Editor:
Jin Xie
Copy Editor:
Tong Wang
Production Editor:
Tong Wang

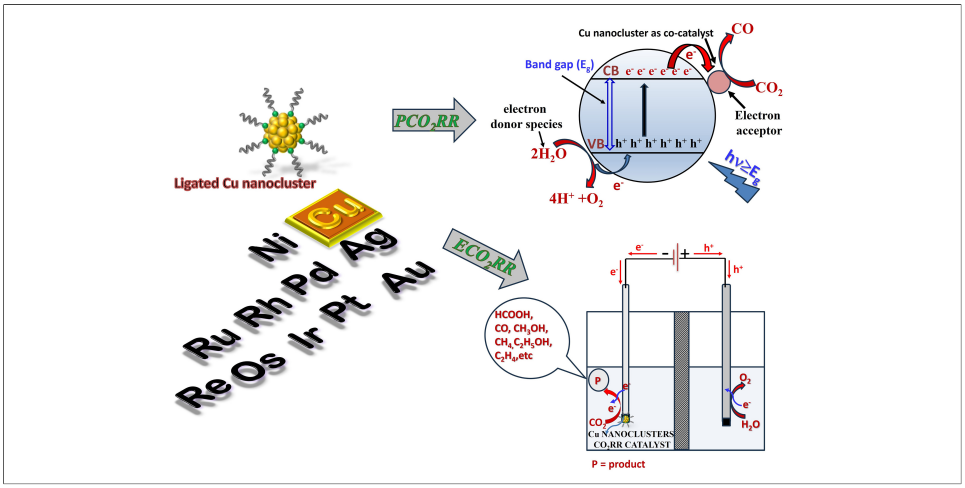

Abstract

CO_2 is a thermodynamically and kinetically stable molecule with its standard Gibbs free energy of formation (ΔG_f°) of -394.4 kJ·mol^{-1} at 298 K and a highly negative first-electron reduction potential (E°) of -1.90 V *vs.* standard hydrogen electrode (SHE) in aqueous solution. Therefore, its thermal reduction requires high temperatures to overcome the unfavorable thermodynamics and kinetics. Even so, electrochemical CO_2 reduction reactions (ECO_2RR) and photochemical CO_2 reduction reactions (PCO_2RR) have been demonstrated to be highly effective in terms of ambient operative conditions, conversion efficiency, and capacity to generate a wide range of value-added carbon-based fuels. However, to drive the ECO_2RR/PCO_2RR, highly efficient and atomically well-defined catalysts with customized optimizations are required. Thanks to the specific and uniform catalytic active sites located on the metal nanocluster surface/interface defined by their precise atomic structure, the ligand-protected atomically precise Cu nanoclusters have been shown to drive the CO_2 reduction reaction (CO_2RR) to various valuable C_1, C_2, and C_{2+} products. The current status of the synthesis and the ECO_2RR and PCO_2RR catalyzed by ligand-protected Cu nanoclusters with precise crystal structures is reviewed in this article.

[1]Department of Chemistry, School of Advanced Sciences, VIT-AP University, Amaravati 522241, India.
[2]School of Chemistry and Chemical Engineering, Inner Mongolia Normal University, Hohhot 010022, Inner Mongolia, China.

***Correspondence to:** Prof. Sachil Sharma, Department of Chemistry, School of Advanced Sciences, VIT-AP University, Amaravati 522241, India. E-mail: sachil.sharma@vitap.ac.in; Prof. Gao Li, School of Chemistry and Chemical Engineering, Inner Mongolia Normal University, Hohhot 010022, Inner Mongolia, China. E-mail: li_gao82@yeah.net

INTRODUCTION

The increased emission of greenhouse gases due to anthropogenic activities will have a substantial impact on long-term climate change. In 2015, the Paris Agreement was adopted to achieve "carbon neutrality" by 2050. Carbon neutrality, i.e., reducing greenhouse gas emissions, including "CO_2 to net-zero," is now a long-term goal shared worldwide. To achieve this, various scientific strategies are being developed. In particular, the adsorption-based capture and conversion of CO_2 into a wide range of carbon-based fuels and value-added organic products, e.g., carbon monoxide, methane, methanol, ethanol, formic acid, ethylene, acetaldehyde, *etc.*, are being investigated, which may help reduce CO_2 emissions while supporting sustainable fuel production[1-6]. However, CO_2 is primarily a thermodynamically and kinetically stable molecule (ΔG_f° = -394.38 kJ·mol^{-1}) with a nonpolar linear structure with a high C=O bond energy (750 kJ·mol^{-1}), making its activation and reduction an extremely challenging process[4]. Hence, a highly efficient catalyst is required to drive its reduction under ambient conditions, which in turn also regulates reaction selectivity, activity, and stability of reaction intermediates for their deep reduction[1-6].

To this end, the early landmark investigations of constant-current electrolysis of CO_2-saturated 0.5 M $KHCO_3$ at 5 mA·cm^{-2} on various electrodes were conducted in 1980s by Hori *et al.*[7-10]. These studies led to an important categorization: Pb, Hg, Tl, In, Sn, Cd, and Bi generate $HCOO^-$; Au, Ag, Zn, Pd, and Ga generate mainly CO; Ni, Fe, Pt, and Ti instead reduce H_2O to H_2; and notably, Cu outperforms other metals by reducing CO_2 beyond CO and HCOOH with significantly high Faradaic efficiency (FE). The above categorization is based on the binding energies of metals with CO_2 reduction reaction intermediates such as *OCHO, *COOH, and *CO. Of note, Cu is the only metal that has a negative adsorption energy for *CO while having positive adsorption energy for *H, responsible for its unique ability to reduce CO_2 deeply beyond 2e$^-$ reduction products. Later, Kuhl *et al.* also examined the electrochemical CO_2 reduction reactions (ECO_2RR) on Cu surfaces in the potential range of -0.6 to -1.2 V *vs.* the reference hydrogen electrode (RHE), where a total of 16 products were detected during CO_2 reduction on polycrystalline Cu[11]. Taking into account the importance of CO* as a reaction intermediate of ECO_2RR, Kuhl *et al.* constructed a volcano curve by plotting the experimental observed ECO_2RR activity and selectivity data against density functional theory (DFT) calculations based on binding energies of CO, which revealed that in comparison to Au, Ag, Zn, Ni and Pt, the Cu metal is placed on top of volcano plot with optimal binding energy of CO for ECO_2RR making it a best catalyst for C-C coupling, facilitating the production of C_{2+} products[12,13]. Following investigations by both Hori *et al.* and Kuhl *et al.*, extensive research has been conducted to understand the reactivity, selectivity, and efficiency of > 2 nm Cu particles for ECO_2RR[3,6-12,14-18]. Thus, cost-effective, abundant, and eco-friendly Cu or Cu-based materials have emerged as highly sought-after catalysts in clean energy infrastructure and sustainable energy production.

However, despite the excellent catalytic properties of these polycrystalline Cu-based nanomaterials (> 2 nm) for ECO_2RR, their surface structure/morphology is often ill-defined and non-uniform, in addition to their inherent particle-size distribution. This results in mixed types of catalytic active sites, leading to significant variations in their catalytic activities, ultimately resulting in the limited selectivity of desired products[2,19]. Moreover, these mixed types of active sites are the major obstacles to understanding the precise mechanism of the CO_2 reduction reaction (CO_2RR) on Cu nanoparticles or Cu-based bulk materials. In contrast to this, the ligand-protected Cu nanoclusters with well-resolved crystal structures at atomic-level precision (i.e., core metal arrangements such as icosahedra, body-centered cubic, face-centered cubic, octahedron, *etc.* surrounded by ligand shells/motifs in specific patterns) in conjunction with their high molecular uniformity (i.e., uniform catalytic active sites) afford higher tunable selectivity of desired products than conventional Cu nanoparticles or other Cu-based bulk materials for electro/photochemical CO_2 reduction[4,20-24]. On top of that, the well-resolved single crystal structures of ligand-protected Cu nanoclusters make them the ideal materials to investigate the structure-property relationships accurately, and hence, the precise details of the

ECO_2RR mechanism can be obtained, which are otherwise ambiguous in the case of Cu nanoparticles. Furthermore, with the advanced knowledge of the precise single-crystal structure of ligand-protected Cu nanoclusters, theoretical studies can further assist the researchers in tailoring the Cu nanocluster-based catalysts for more efficient ECO_2RR and PCO_2RR.

Although significant success has been achieved in CO_2 reduction to CO over atomically precise Au and Ag nanoclusters[2,25-27], the optimized design of these catalysts ensuring high efficiency and selectivity remains challenging. Here, Cu nanoclusters have emerged as promising catalysts for ECO_2RR/PCO_2RR. As discussed, Cu binds CO with moderate interactions, i.e., not strong enough to desorb from the catalyst surface yet strong enough to stabilize reaction intermediates, thereby enabling its further reduction to diverse value-added products beyond CO[3,6-13]. A second distinct feature of Cu is its ability to exist in various oxidation states (0/+1/+2), which significantly impacts the products of multielectron CO_2 reduction. Notably, Cu in 0 and +1 oxidation states has been observed in ligand-protected Cu nanoclusters[21]. However, the main disadvantage of ligand-protected atomically precise Cu nanoclusters compared to Au and Ag nanoclusters is their instability, plausibly owing to their lower standard reduction potential (Cu^+/Cu = +0.52 V and Cu^{2+}/Cu = +0.34 V) than Ag (Ag^+/Ag = +0.80 V) and Au (Au^+/Au = +1.83 V and Au^{3+}/Au = +1.50 V)[28]. By addressing these challenges and using innovative synthesis strategies, the full potential of atomically precise Cu metal nanoclusters as next-generation CO_2 reduction catalysts can be achieved. Thus far, a relatively small number of ligand-protected Cu nanoclusters have been identified as catalysts for electro/photochemical reduction of CO_2. This article reviews these reported systems as next-generation CO_2 reduction catalysts.

SYNTHESIS

Monoatomic ligand-protected Cu nanoclusters

Basically, three types of ligand-protected homoatomic Cu nanoclusters have been reported[28]: (i) Cu(I) hydride nanoclusters; (ii) hydride-free Cu(I) nanoclusters; and (iii) Cu nanoclusters with partial Cu(0) character. Dhayal *et al.* started off the synthesis of Cu(I) hydride nanoclusters using a nonaqueous solution of a reducing agent, Cu(I) precursor, and dichalcogen ligands[29]. They also generated analogous hydride-free Cu(I) nanoclusters without $[BH_4]$. Following this, Cu(I) nanoclusters with and without hydrides were synthesized by other research groups through the reduction with a nonaqueous $[BH_4]^-$ solution and without $[BH_4]^-$, respectively, using a single or a mix of protecting ligands[28]. However, Nematulloev *et al.* reported a hydride-free thiolate- and phosphine-protected Cu(I) nanocluster with the formula $[Cu_{15}(PPh_3)_6(PET)_{13}]^{2+}$ (PET: 2-phenylethanethiol) through the reduction with a nonaqueous $[BH_4]^-$ solution[30]. Notably, the hydride- and hydride-free thiolate-protected Cu(I) nanoclusters have been produced using an aqueous $[BH_4]^-$ solution. For example, Li *et al.* synthesized $[Cu_{11}(TBBT)_9(PPh_3)_6]^{2+}$ (TBBT: 4-tert-butylbenzenethiolate)[31], and another example of a hydride-free Cu(I) cluster, $[Cu_8(SPh)_8(Ph_3P)_4]$, using the ice-cold aqueous solution of $NaBH_4$, was reported by Ke *et al.*[32]. Tang *et al.* introduced a novel two-step addition of aqueous $NaBH_4$ at two different temperatures to obtain a high-nuclearity thiolated $[Cu_{75}(S\text{-}adm)_{32}]^{2+}$ nanocluster (adm: adamantane)[33]. Interestingly, Cu(I)-thiolate nanoclusters with hydride having compositions: $[Cu_{14}(S\text{-}tert\text{-}Bu)_3(PPh_3)_7H_{10}]$, $[Cu_{18}H(PET)_{14}(PPh_3)_6(SCN)_3]$, $[Cu_{25}H_{10}(SPhCl_2)_{18}]^{3-}$ were also obtained using aqueous $NaBH_4$[34-36]. So, there is no general protocol to use an aqueous/non-aqueous solution of $NaBH_4$ to produce the desired hydride or hydride-free Cu nanoclusters. Notably, the synthesis of Cu nanoclusters with Cu(0) character has been challenging owing to the intrinsic high reactivity of Cu(0). A gradient reduction strategy has recently been applied by Han *et al.* to synthesize $[Cu_{23}(tert\text{-}BuC{\equiv}C)_{13}(CF_3COO)_6]$ having partial Cu(0)[37]. Nguyen *et al.* also reported $[Cu_{25}H_{22}(PPh_3)_{12}]Cl$ nanoclusters with the presence of partial Cu(0)[38]. Additionally, $[Cu_{18}H_3(S\text{-}Adm)_{12}(PPh_3)_4Cl_2]$[39], $[Cu_{14}(C_2B_{10}H_{10}S_2)_6(CH_3$

$CN)_8$][40], $[Cu_{31}(4\text{-MeO-PhC}\equiv C)_{21}(dppe)_3](ClO)_4$[41], and $[Cu_{23}(SR)_{18}(TPP)_6](SbF_6)$ with a $Cu@Cu_8$ body-centred cubic core[42], each having partial Cu(0) character, and $[Cu_{23}H_4(SC_7H_7)_{18}(PPh_3)_6]$[43] with a central Cu(0) atom are also reported.

Copper-based alloy nanoclusters

The co-reduction and galvanic/anti-galvanic reduction methods are potential routes to synthesize heteroatom-doped Cu-M (M: Au/Ag/Pd/Pt) alloy nanoclusters with enhanced stability[44]. Significant progress has been made on metal alloy nanoclusters involving group 11 metals based on d^{10}-d^{10} metallophilicity. Examples with reference to CO_2RR catalysis include $[Ag_{15}Cu_6(C\equiv CR)_{18}(DPPE)_2]^-$ [HC≡CR: 3,5-bis(trifluoromethyl)phenylacetylene; DPPE: 1,2-bis(diphenylphosphino)ethane][45], and $[Cu_{14}Ag_6(TC4A)_2(PhC\equiv C)_{12}(MeOH)]$ (TC4A: thiacalixarene[4]arene; PhC≡C: phenyl acetylene)[46]. However, the synthesis of alloy nanoclusters of Cu with groups 9 and 10 metals is challenging due to large differences in atomic radii and standard reduction potentials. Examples include $[Pt_2Cu_{34}(PET)_2Cl_4]^{2-}$, and $[Cu_{16}Pd_1L_{10}(PPh_3)_2(PZ)_6]$ [PZ: 3,5-$(CF_3)_2$Pyrazolate and L: 4-CH_3OPhCC$^-$][47,48].

ELECTROCHEMICAL CO_2 REDUCTION REACTIONS (ECO_2RR)

Fundamental principle

The first step of ECO_2RR is the CO_2 activation, i.e., the diffusion of linear CO_2 to a metal surface followed by its adsorption to form radical anion $CO_2^{\cdot-}$ (with bent geometry) through direct one-electron reduction. However, this step requires very high energy to overcome the activation barrier indicated by a high negative standard reduction potential E^o = -1.90 V *vs.* standard hydrogen electrode (SHE) in water (pH = 7) and E^o = -1.97 V *vs.* SHE in an aprotic solvent such as N,N-dimethyl formamide (DMF) on a non-catalytic or poorly catalytic electrode surface[49-51]. To avoid this high-energy intermediate, the electrocatalysts offer a less negative and more favorable overpotential using an alternative proton-coupled electron transfer pathway (PCET) [Figure 1][21,51,52]. CO_2 can bind to the catalyst surface either through carbon coordination, forming the *COOH intermediate, or through oxygen coordination, forming the HCOO* intermediate. The *COOH further undergoes PCET to produce a *CO intermediate, which either desorbs from the catalyst surface as CO or can undergo further PCET to generate CH_4 and CH_3OH through the *COH and *CHO intermediates. However, the HCOO* intermediate generates HCOOH as a final product via PCET. Furthermore, Cu has the potential to facilitate the C-C coupling reaction owing to its moderate binding to *CO, thereby allowing it to remain on Cu long enough to interact with another molecule. Basically, C_2 product pathways are more complex, in which the *COCO, *COCHO, and *COCOH are common C_2 intermediates [Figure 1][21]. The *COCO is formed by coupling between two *CO intermediates, while *COCHO and *COCOH are formed either by protonation of *COCO or reaction of *CO either with *COH or *CHO intermediates. Recently, considerable progress has been made in understanding the synergistic effects in ECO_2RR to promote the multi-carbon product formation[53].

Ligand-protected Cu nanocluster for ECO_2RR

HCOOH selective ECO_2RR: role of lattice hydrides

In their pioneering work, Tang *et al.* presented the "lattice hydride mechanism" in 2017[54] to explain the ECO_2RR over $[Cu_{32}(H)_{20}\{S_2P(O^iPr)_2\}_{12}]$ (Cu_{32}) nanoclusters at low overpotentials. Cu_{32} features a hexacapped pseudo-rhombohedral metal core of 14 Cu atoms packed between two triangular cupola fragments of Cu atoms, and overall Cu_{32} is stabilized by 1,2-dithiophosphate ($S_2P(O^iPr)_2$) ligands and 20 hydride ligands with three kinds of bridging coordination patterns [Figure 2A]: 12μ_3-H (lattice hydrides), 6μ_4-H (interstitial hydrides), and 2μ_5-H (interstitial hydrides). The 12μ_3-H lattice hydrides are further sorted into three μ_3-H_1, two μ_3-H_2, four μ_3-H_3, and two μ_3-H_4. As per DFT calculations, CO_2 adsorbed at the most favored site at μ_3-H_1, followed by reduction by hydride addition (μ_3-H_1) to C of CO_2 to form adsorbed HCOO* (ΔG^0 = 0.32 eV),

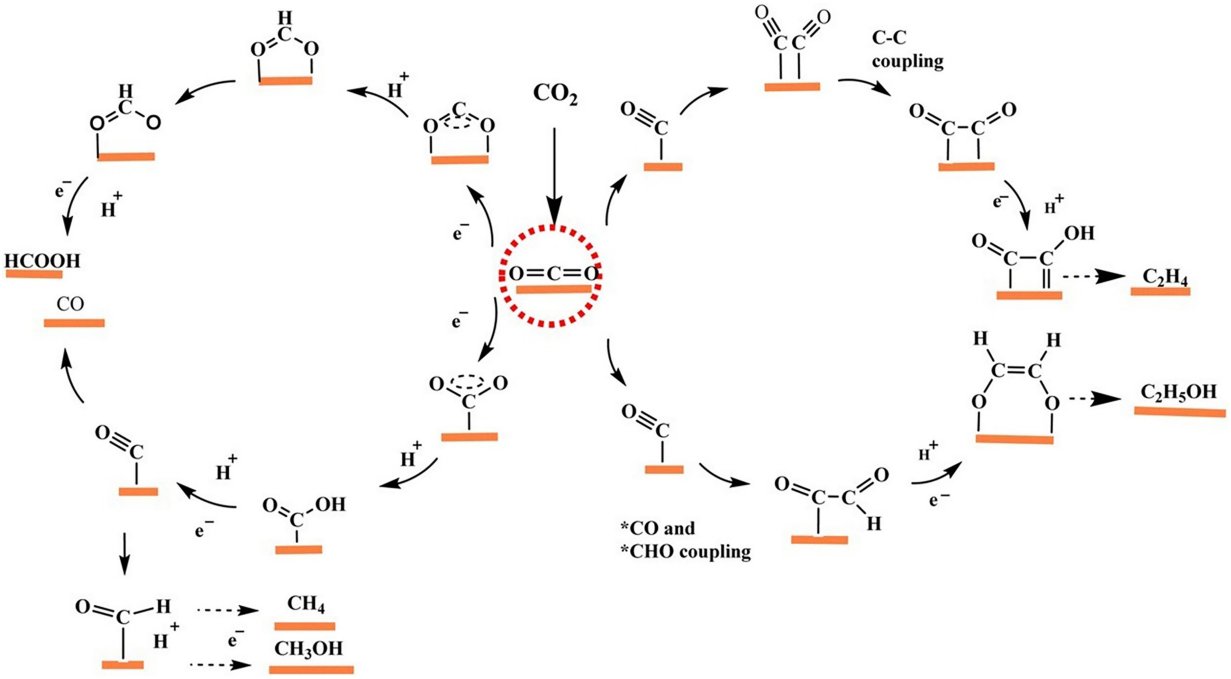

Figure 1. Reaction mechanistic pathways of ECO_2RR. This figure is reproduced with permission from Ref.[21]. © The Royal Society of Chemistry 2025.

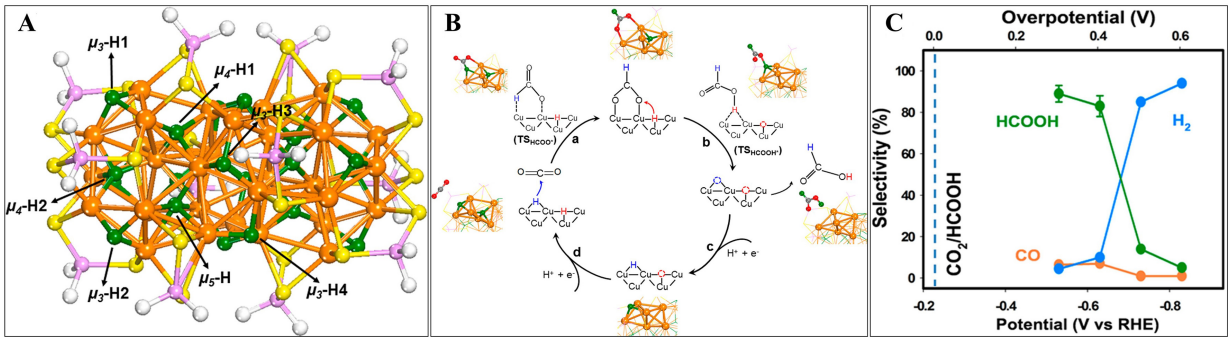

Figure 2. (A) Structure of Cu_{32}; (B) Lattice hydride mechanism of HCOOH generation during CO_2 reduction on Cu_{32}; (C) Product selectivity for H_2, HCOOH, and CO at different overpotentials. Color code: Cu, orange; hydride, green; oxygen, red; carbon, gray. This figure is reproduced with permission from Ref.[54]. Copyright © 2017 American Chemical Society. RHE: Reversible hydrogen electrode.

owing to attraction between negatively charged hydride and positively charged C of CO_2 to form $Cu_{32}H_{19}L_{12}$-HCOO*. It is further succeeded by the addition of another hydride (μ_4-H_1) to finally form the HCOOH product (G = 0.07 eV) with FE of 90%. These two hydride vacancies of $Cu_{32}H_{18}L_{12}$ are regenerated by two back-to-back electrochemical proton reductions to resume the catalytic cycle [Figure 2B]. Furthermore, the first hydride transfer revealed that higher overpotentials of +0.81 V and +0.6 to +1 eV, respectively, are needed for competing CO formation and the hydrogen evolution reaction (HER) relative to HCOOH formation occurring at low overpotentials (+0.32 V) and thus cannot compete with HCOOH formation. The controlled potential electrocatalysis experiments using Cu_{32} in 0.1 M $KHCO_3$ and 0.4 M KCl (pH = 6.8) on the Cu_{32}/C/GDL electrode supported the theoretical results. Cu_{32} mainly produced HCOOH at low overpotentials (89% at +0.3 V and 83% at +0.4 V) with a small amount of CO and H_2 [Figure 2C]. At overpotentials above +0.5 V, H_2 was generated predominantly (85% at 0.5 V and 94% at +0.6 V).

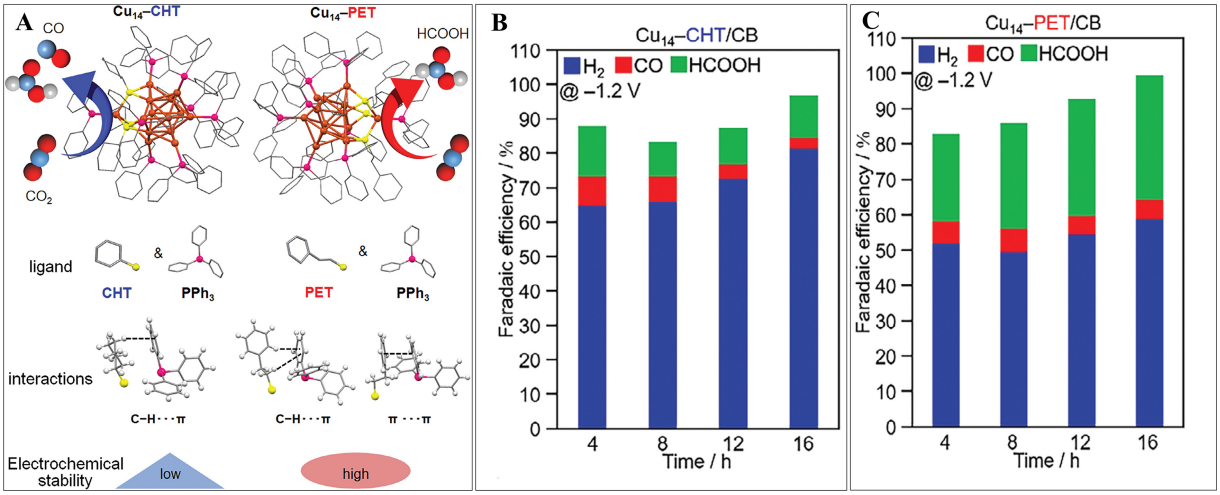

Figure 3. (A) Structures of Cu_{14}-CHT and Cu_{14}-PET exhibiting different interactions; time-dependent FE for ECO_2RR products on (B) Cu_{14}-CHT/CB, and (C) Cu_{14}-PET/CB. This figure is reproduced with permission from Ref.[55]. Licensed under CC BY 4.0. FE: Faradaic efficiency.

HCOOH selective ECO_2RR: ligand effect

To investigate the effect of ligands on ECO_2RR, Shingyouchi *et al.* prepared Cu_{14} nanoclusters with compositions $[Cu_{14}(CHT)_3(PPh_3)_8H_{10}]^+$ (Cu_{14}-CHT) and $[Cu_{14}(PET)_3(PPh_3)_8H_{10}]^+$ (Cu_{14}-PET) protected by cyclohexane thiolate (CHT) and 2-phenylethane thiolate (PET)[55]. Structure-wise, both nanoclusters have distorted fcc (face-centered cubic) structures equipped with an inner Cu_6 octahedral core and outer Cu_8 cube. These overall distorted structures are stabilized due to various intracluster interactions, e.g., C-H---π interactions in Cu_{14}-CHT and C-H---π interactions and T-shaped π-π interactions in Cu_{14}-PET [Figure 3A]. The smaller Cu-Cu and Cu-S average distances in Cu_{14}-PET resulted in a reduction in its size and inner cuprophilic interactions, enhancing its stability, which influenced the stability of reaction intermediates during ECO_2RR and determined the selectivity of the product.

HCOOH was the main product using both Cu_{14} clusters in the potential range of -0.8 V to -1.4 V (*vs.* RHE). Briefly, for Cu_{14}-CHT/CB, FE_{HCOOH} and FE_{CO} were ≈31% and ≈8% and for Cu_{14}-PET/CB, FE_{HCCOH} and FE_{CO} were ≈39% and ≈2% at -1.2 V [Figure 3B and C], respectively, supported by higher current densities (J_{COOH}) displayed by latter. The higher stability of reaction intermediate HCOO* than *COOH in Cu_{14}-PET prefers production of highly selective HCOOH over CO. Cu_{14}-CHT clusters showed an increase in HER, whereas Cu_{14}-PET maintained HER and CO production while enhancing the HCOOH production over extended time[55]. The increase in HER during prolonged electrochemical exposure is attributed to the aggregation of Cu_{14}-CHT.

HCOOH selective ECO_2RR: effect of metal core structure

To investigate effect of isomers for ECO_2RR, Liu *et al.* synthesized Cu nanoclusters with compositions $Cu_8(H)(L1)_6PF_6$ (Cu_8-1), $Cu_8(^tBuS)_4(L1)_4$ (Cu_8-2), and $Cu_8(^tBuS)_4(L2)_4$ (Cu_8-3) (L1: 9H-carbazole-9-carbodithiol; L2: o-ethyl carbonodithiol)[56]. Cu_8-1 possesses a cubic kernel protected by L1-type ligands [Figure 4A], and upon partial replacement of L1 or L2 by $^tBuS^-$, Cu_8-2 and Cu_8-3, possessing ditetrahedron kernels, were prepared, respectively [Figure 4B and C]. According to the space-filling model, all Cu_8 clusters with a low number of ligands covering Cu atoms act as active sites[56].

Linear sweep voltammetry (LSV) curves of all Cu_8 clusters in CO_2-saturated solution exhibited high current density, indicating their activity for ECO_2RR. The lower onset potentials for Cu_8-2 and Cu_8-3 (-0.6 V and -0.48 V, *vs.* RHE, respectively) than Cu_8-1 (-0.71 V *vs.* RHE) suggested the lower energy barrier of ECO_2RR

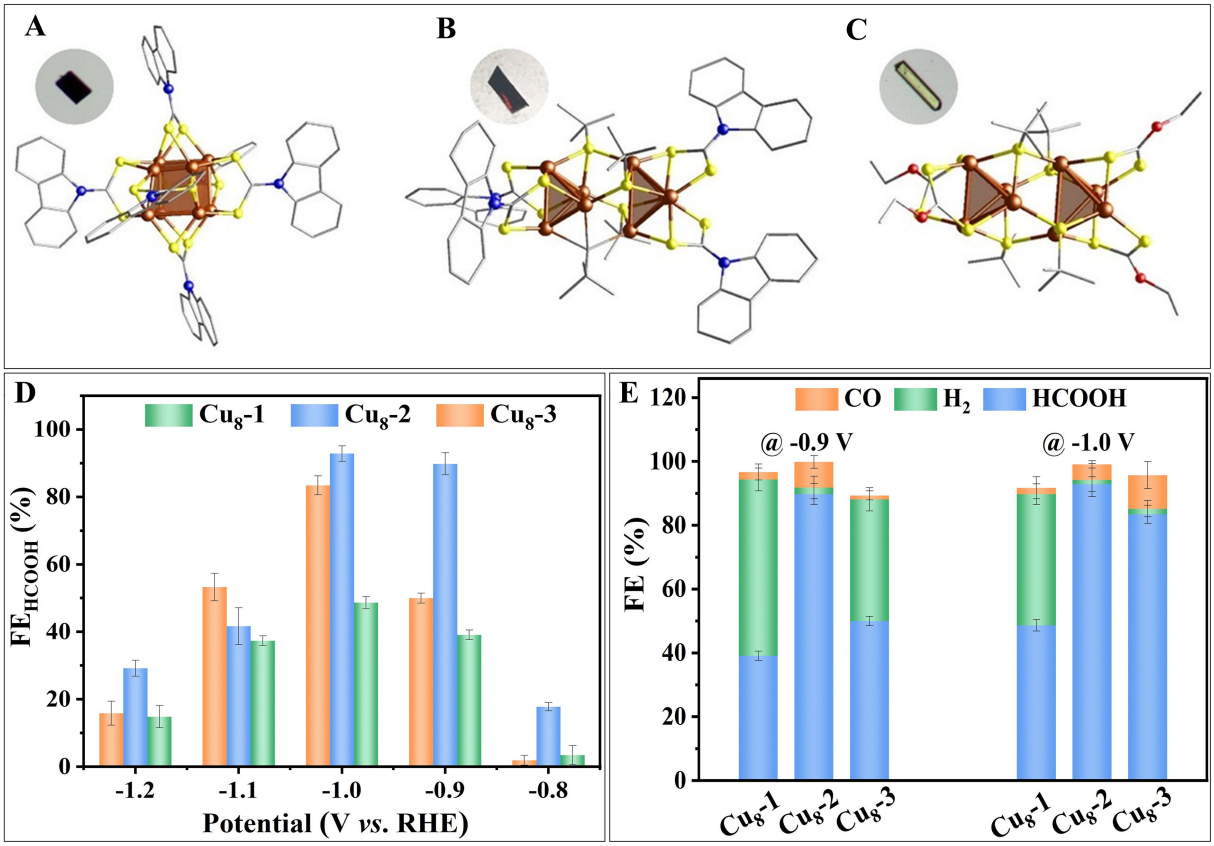

Figure 4. Total structures of (A) Cu_8-1, (B) Cu_8-2, and (C) Cu_8-3; (D) FE_{HCOOH} of Cu_8-1, Cu_8-2, and Cu_8-3 at various applied potentials; (E) FE_{HCOOH}, FE_{CO}, and FE_{H2} at -0.9 and -1.0 V on Cu_8-1, Cu_8-2, and Cu_8-3 clusters. This figure is reproduced with permission from Ref.[56], © 2022 Wiley-VCH GmbH.

for ditetrahedron kernels[56]. The electrochemical performance in the range of -0.8 to -1.2 V *vs.* RHE yielded H_2, CO, and HCOOH with total FE > 90%. The ditetrahedron Cu_8 clusters exhibited higher FE_{HCOOH} and selectivity than cubic Cu_8 in this potential range as shown in Figure 4D. In more detail, as potential tuned from -0.8 to -1.0 V, HCOOH selectivity for all Cu_8 clusters increased, accompanied by a notable decrease beyond -1.0 V, where H_2 became the primary product. The FE_{HCOOH} values for ditetrahedron Cu_8-2, shown in Figure 4E, were evaluated to be 90% and 92% at -0.9 and -1.0 V, respectively, which were 2 times higher than Cu_8-1 clusters (39.1% and 48.6% at -0.9 and -1.0 V, respectively), supported by higher J_{COOH} values for Cu_8-2 and Cu_8-3. Of note, the slight difference in activities between the ditetrahedron Cu_8-2 and Cu_8-3 owes to the ligand effect. The chronoamperometric measurements revealed the relatively high electrochemical stability of Cu_8-2 and Cu_8-3 under the operating conditions for 8 h[56].

As per DFT calculations, the difference in CO_2RR activity for Cu_8-1 and Cu_8-2 is ascribed to distortion caused by the corner site in the latter [Figure 5A and B], supported by the potential energy diagram showing suppression of HER for Cu_8-2 [Figure 5C]. These results were consistent with the experimental findings shown in Figure 4E. The CO_2RR process shown in Figure 5D, where the conversion of $*CO_2$ to HCOO* occurs with a lower free energy for Cu_8-2 than Cu_8-1, further proves the former's higher reactivity and selectivity.

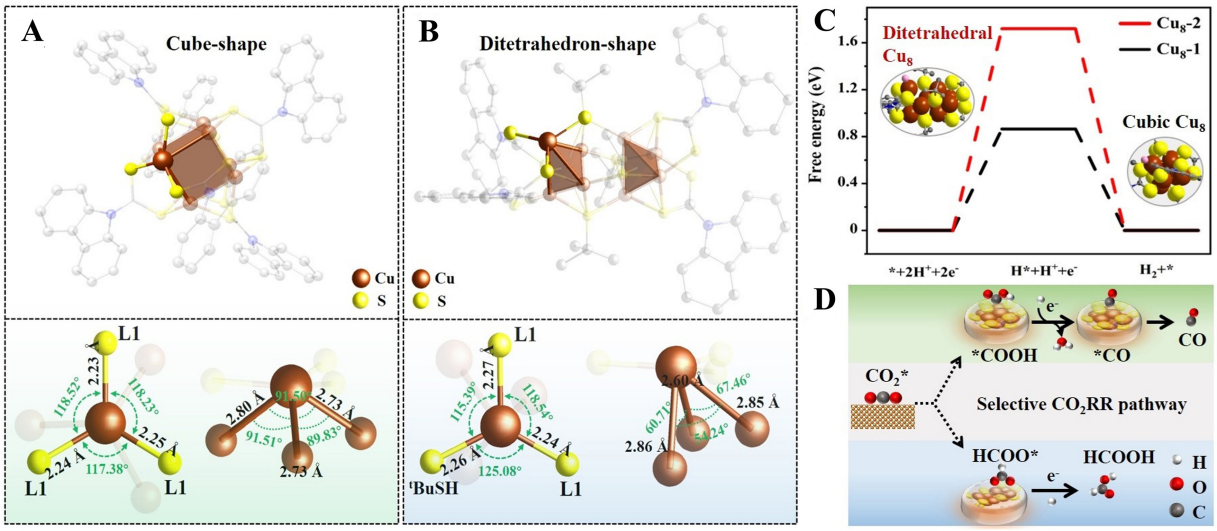

Figure 5. Corner site structures for Cu_8 nanoclusters with (A) cubic and (B) ditetrahedron kernels along with coordination environment; (C) Potential barrier diagram for Cu_8-2 and Cu_8-1 for HER; (D) CO_2RR process over Cu_8 nanoclusters for CO and HCOOH products. This figure is reproduced with permission from Ref.[56], © 2022 Wiley-VCH GmbH. HER: Hydrogen evolution reaction.

HCOOH selective ECO$_2$RR: role of structural arrangements

Biswas *et al.* recently fabricated a highly stable $[Cu_{23}H_4(SC_7H_7)_{18}(PPh_3)_6]$ (Cu_{23}) (SC_7H_7: *p*-toulenethiolate) nanocluster via fusion of two $[Cu_{12}H_2(SC_7H_7)_7(PPh_3)_3]$ subunits sharing a Cu(0) atom [Figure 6A][43]. The remarkable stability of Cu_{23} motivated the authors to investigate Cu_{23}/CB for ECO$_2$RR. FE data in Figure 6B indicated a maximum FE_{HCOOH} ~26% at -1.2 V along with FE_{H2} ~42% and minor CO for Cu_{23}. While 30 nm Cu particles prepared with the same precursor via calcination displayed FE_{H2} ~80% at -1.0 V, indicating uncontrolled competitive HER along with FE_{HCOOH} ~8% and FE_{CO} ~6%, underlining the superior HCOOH selectivity of Cu_{23}. DFT revealed antenna-like Cu_3 units on both sides of the overall geometry, forming the more favorable hollow triangular prism-like sites for H_2 adsorption in line with high HER at low overpotential [Figure 6C]. Additionally, these sites also act as potential active sites for CO_2RR [Figure 6C], and among their two investigated pathways, the *HCOOH (via HCOO* intermediate) pathway is preferred over the *COOH pathway as per their energy profiles [Figure 6D], in agreement with selective production of HCOOH on Cu_{23}.

Ethylene selective ECO$_2$RR catalysis: ligand effect

Han *et al.* synthesized two Cu nanoclusters with the compositions $[Cu_{17}H_6(NHC^H)_4(dppm)_4](PF_6)_3(MeCN)_3(CH_2Cl_2)(Et_2O)$ (Cu17a) [NHC^H: 1,3-diprop-2-ynyl-1H-imidazol-3-ium hexafluorophosphate; dppm: Bis(diphenylposphino)methane] with its crystal structure [Figure 7A] and $Cu_{17}H_6(NHC^{ph})_4(dppm)_4](PF_6)_3(MeCN)(CH_3OH)$ (Cu17b) [NHC^{Ph}: 1,3-bis(2-propyn-1-yl)-1H-benzoimidazol-3-ium hexafluorophosphate]. Both Cu17a and Cu17b feature a $Cu_{17}H_6$ square orthobicupola as a common core, shown in Figure 7B[57]. The σ and π bonding between Cu and N-heterocyclic carbene (NHC) ligands [Figure 7C] provides high stability to both these Cu17 clusters, and moreover, the distinctive coordination pattern (μ_7-η_σ^1:η_σ^1:η_σ^1:η_σ^1:η_π^2:η_π^2) of the NHC ligand exposes the neighboring Cu atoms as active sites for CO_2RR.

Comparing the structures of Cu17a [Figure 7A] and Cu17b[57], a ligand effect was noticed on ECO$_2$RR activity due to minimal steric hindrance for CO_2 adsorption on Cu17a compared to Cu17b. The more positive onset potential and higher cathodic current density observed for Cu17a indicate their higher activity towards CO_2

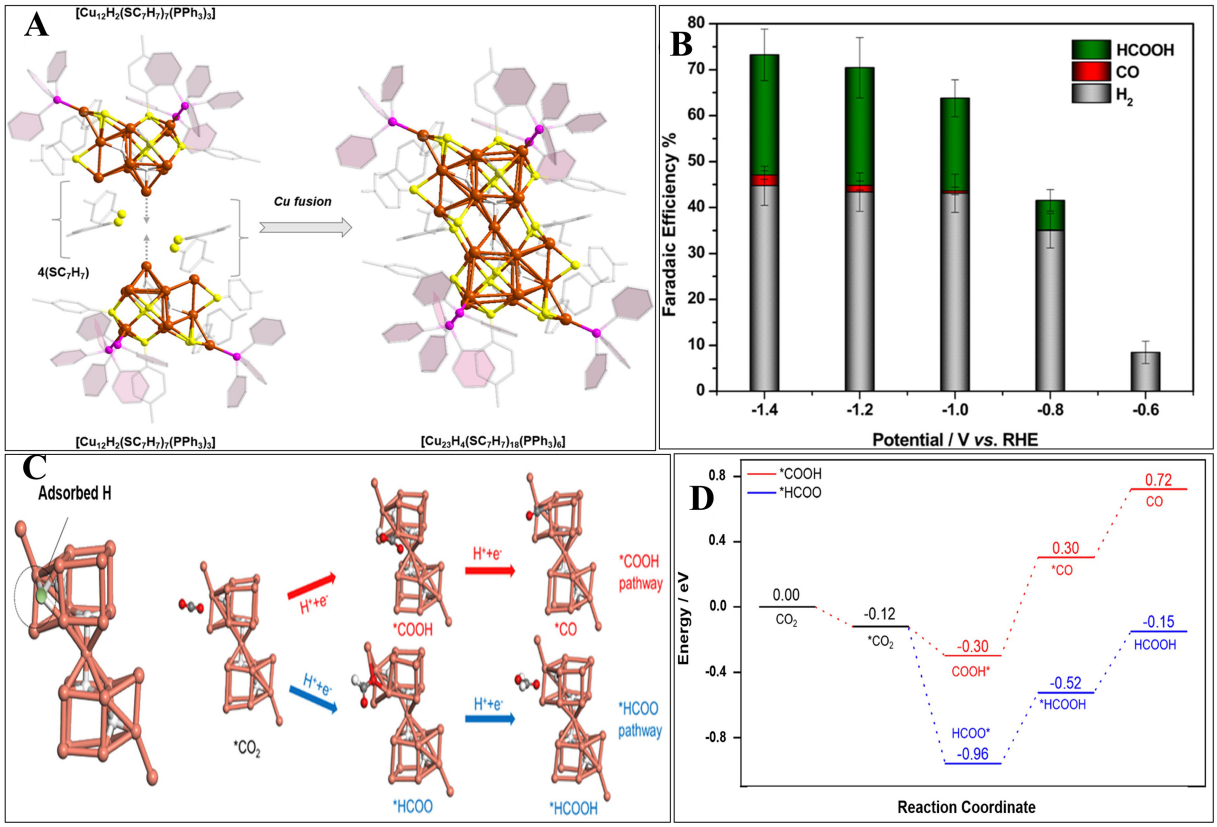

Figure 6. (A) Structure of Cu_{23} nanocluster formed upon fusion of two identical Cu subunits; (B) FEs of ECO_2RR products on Cu_{23}/CB at different applied potentials; (C) Scheme of H adsorption on active site; (D) DFT computed energy values of plausible pathways. Color code: Cu, brown; S, yellow; P, violet; H, white; C, gray. This figure is reproduced with permission from Ref.[43], Copyright © 2025 The Authors. FE: Faradaic efficiency; DFT: density functional theory.

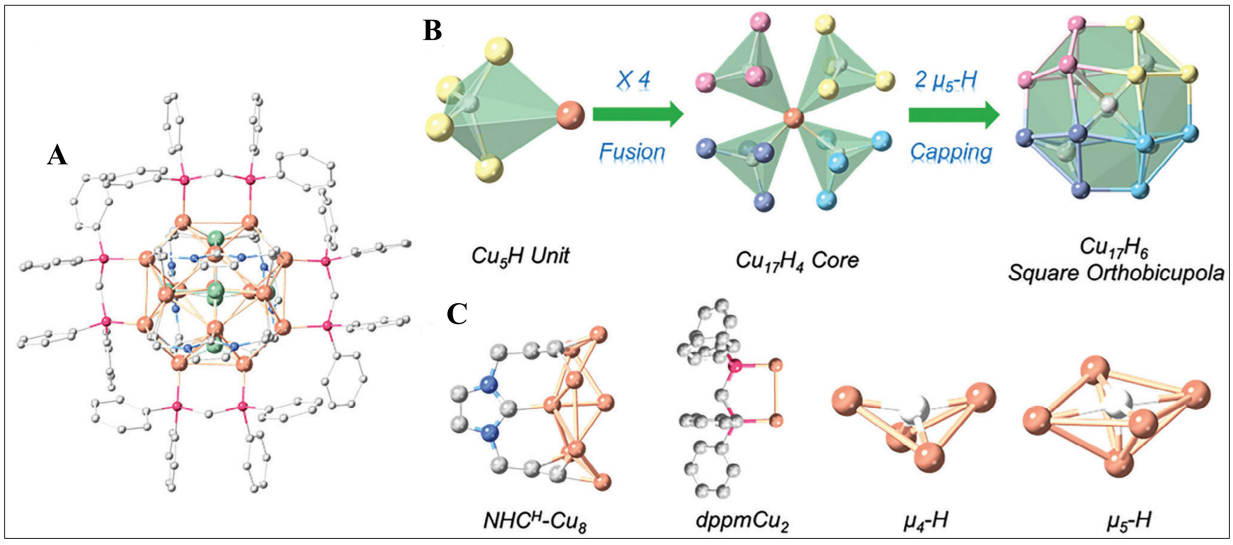

Figure 7. (A) Total structure of Cu17a; (B) Formation of $Cu_{17}H_6$ square orthobicupola by vertex sharing of four Cu_5H triangular bipyramids; (C) Ligand coordination pattern in Cu17a. Color code: Cu, orange/yellow/pastel cyan/pastel blue/pastel magenta; N, blue; C, gray; P, rose red; H, green/white. This figure is reproduced with permission from Ref.[57], © 2025 Wiley-VCH GmbH.

RR than Cu17b[57]. For Cu17a, FE_{CO} reached approximately 91% at -0.37 V [Figure 8A], exceeding the values reported for the Cu nanocluster-based electrocatalysts[58]. In contrast, Cu17b displayed poor catalytic activity,

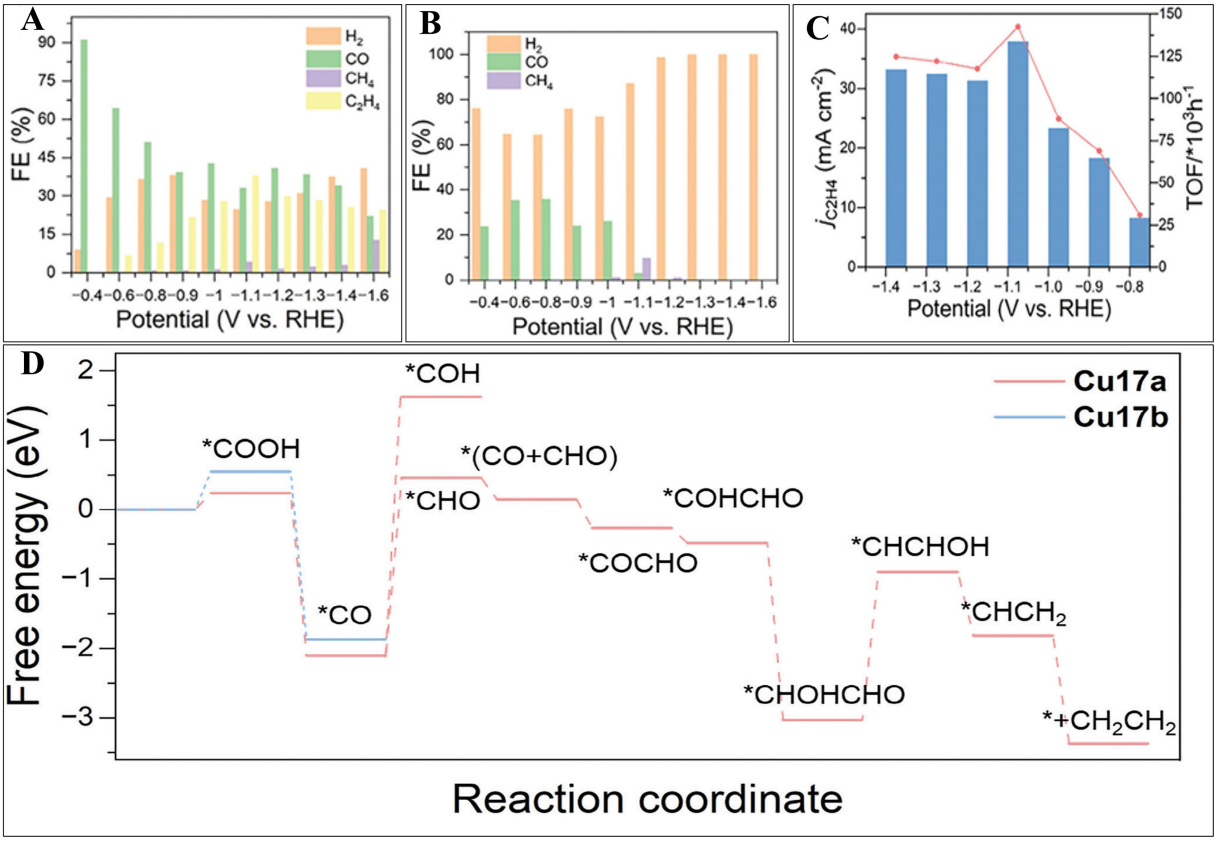

Figure 8. FE of ECO_2RR products over (A) Cu17a and (B) Cu17b; (C) Potential-dependent J_{C2H4} and TOF of Cu17a; (D) Free energy diagrams of ECO_2RR pathways for Cu17a and Cu17b. The asterisk (*) is standard notation for adsorbed species on catalyst surface. This figure is reproduced with permission from Ref.[57], © 2025 Wiley-VCH GmbH. RHE: Reversible hydrogen electrode; FE: Faradaic efficiency; TOF: turnover frequency.

with CO being the main product across the potential range from -0.37 to -1.07 V, with maximum FE_{CO} ~36% [Figure 8B]. As more negative potential is applied, FE_{C2H4} is enhanced initially and then decreased beyond -1.1 V for Cu17a [Figure 8C].

Due to the competitive HER, H_2 was the main product at high potentials [Figure 8A and B]. The attenuated total reflectance surface-enhanced infrared absorption spectroscopy (ATR-SEIRAS) showed the broad peak of adsorbed water molecules at 1,670 cm^{-1}, which was used to perform proton-coupled electron transfer. The peak at 1,366 cm^{-1}, owing to *COOH, suggested CO_2 hydrogenation followed by adsorption of *CO. Further, peaks of *OCCHO at 1,498 cm^{-1} and 1,316 cm^{-1} confirm its significance as an intermediate in the C-C coupling process. Thus, the formation of the C_2H_4 product is facilitated by Cu17a. The optimized space-filling model of these clusters revealed the cavity between two parallel NHC ligands, resulting in exposing two adjacent Cu atoms as potential active sites. The free energy diagram [Figure 8D] explains the thermodynamic favorability of CO_2 reduction by suggesting that surface ligands with less steric hindrance assisted the substrate adsorption. Hence, Cu17a displays more effective CO_2 adsorption with a free energy of -0.56 eV, which is less than -0.23 eV of Cu17b.

Methanol selective ECO_2RR catalysis: defect induced effects

Biswas *et al.* reported ECO_2RR driven selective synthesis of methanol over defect-induced nanocluster $[Cu_{58}H_{20}(SPr)_{36}(PPh_3)_7]^{2+}$ (Cu_{58}-I) (Pr: $CH_2CH_2CH_3$; PPh_3: triphenylphosphine)[59]. Cu_{58}-I, lacking one PPh_3 ligand, was synthesized using the protocol reported for the synthesis of regular

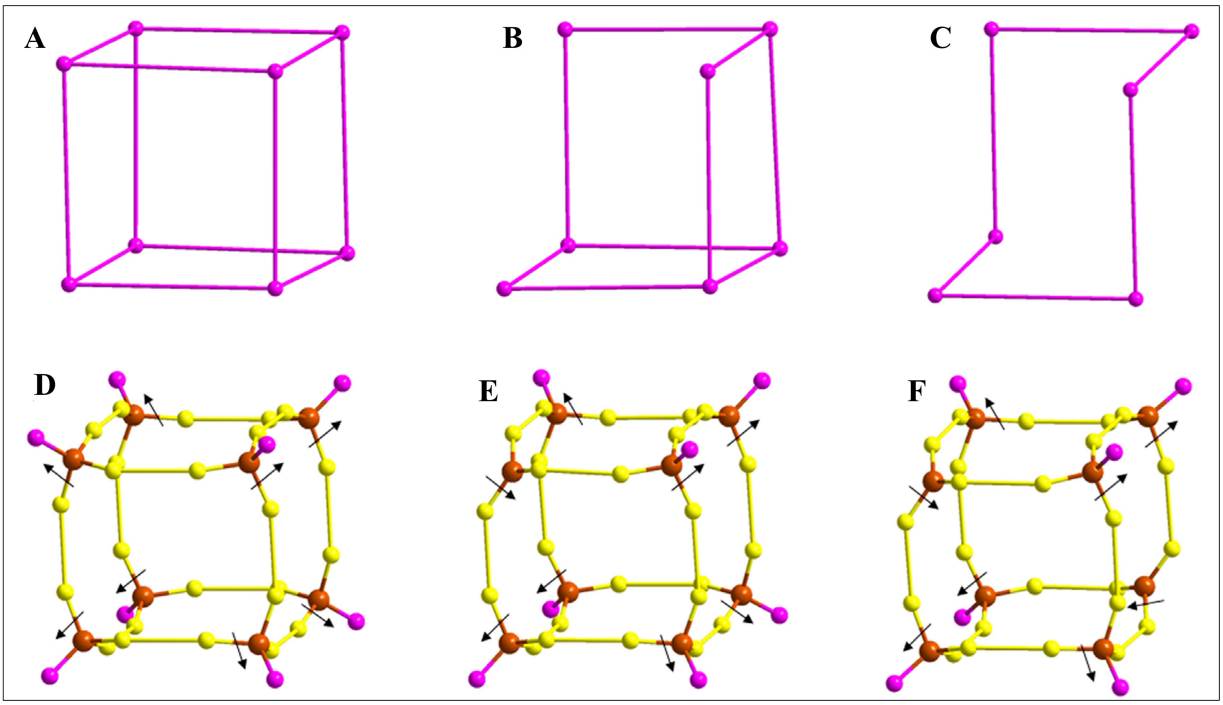

Figure 9. (A) Complete cubic P_8 shell of Cu_{58}; (B) Partial cubic P_7 shell of Cu_{58}-I; (C) Partial P_6 shell of Cu_{58}-II; Typical outward and inward directional arrangement of the cubic shell associated with attached ligands in (D) Cu_{58}, (E) Cu_{58}-I, and (F) Cu_{58}-II, respectively. Color code: Cu, brown; S, yellow; P, violet. This figure is reproduced with permission from Ref.[59], licensed under CC BY 4.0.

$[Cu_{58}H_{20}(SPr)_{36}(PPh_3)_8]^{2+}$ (Cu_{58}) with nested Keplerian architecture[59,60]. The further dissociation of a PPh_3 ligand from Cu_{58} was found difficult; however, this was achieved upon replacing the SPr with SEt (Et: CH_2CH_3), resulting in another defect-induced nanocluster $[Cu_{58}H_{20}(SEt)_{36}(PPh_3)_6]^{2+}$ (Cu_{58}-II)[59]. The Keplerian architecture of all three above Cu_{58} nanoclusters exhibits a Cu_8 cubic core confined by four concentric Cu(I) shells: the innermost Cu_6 octahedron shell, followed by the Cu_{24} rhombicuboctahedron shell, followed by the Cu_{12} cuboctahedron shell, followed by the outermost Cu_8 cubic shell[59,60]. Notably, a key difference was found in the arrangement of PPh_3 ligands in Cu_{58} and Cu_{58}-I. Unlike in Cu_{58}, where the eight PPh_3 ligands form a complete cubic ligand shell (P_8) around nanoclusters [Figure 9A], one and two phosphine ligand vacant sites were found in cubic P_8 ligand shells of Cu_{58}-I [Figure 9B] and Cu_{58}-II [Figure 9C], respectively, resulting in corresponding one and two exposed vertex Cu sites. The construction of the P_8 ligand shells depends on Cu-P bond formation involving Cu(I) atoms of the outermost Cu_8 cubic shell [Figure 9D-F]. As a result, the following distortions modify the internal cationic geometry, leading to strong cuprophilic interactions at defect sites, which in turn impacts the product selectivity.

Cu_{58}-II with more defects showed the highest reduction current, followed by less defect-induced Cu_{58}-I, followed by regular Cu_{58} at -0.9 V. However, all Cu_{58} nanoclusters yielded different selective products during ECO_2R. For instance, H_2, CO, and CH_3OH are key products for Cu_{58}-I [Figure 10A], while H_2, CO, and HCOOH for Cu_{58}-II [Figure 10B]. FE analysis revealed that HER was dominant (FE_{H_2} > 50%) for Cu_{58}-II, with a higher number of defects resulting in more exposed Cu vertices and edges. The Cu_{58}-I, with relatively fewer distortions and exposed Cu sites, selectively yielded CH_3OH with FE_{CH_3OH} ≈54% at -0.7 V [Figure 10A]. On the other hand, regular Cu_{58} produced only CO due to few active sites [Figure 10C].

The computational hydrogen electrode method revealed that the formation of *COOH is more favorable than *HCOO since it is less uphill for Cu_{58}-1 than Cu_{58} in the energy level diagram [Figure 10D]. Subsequently, the formation of *CO from *COOH occurs, and after H_2O desorption, *CO converts into

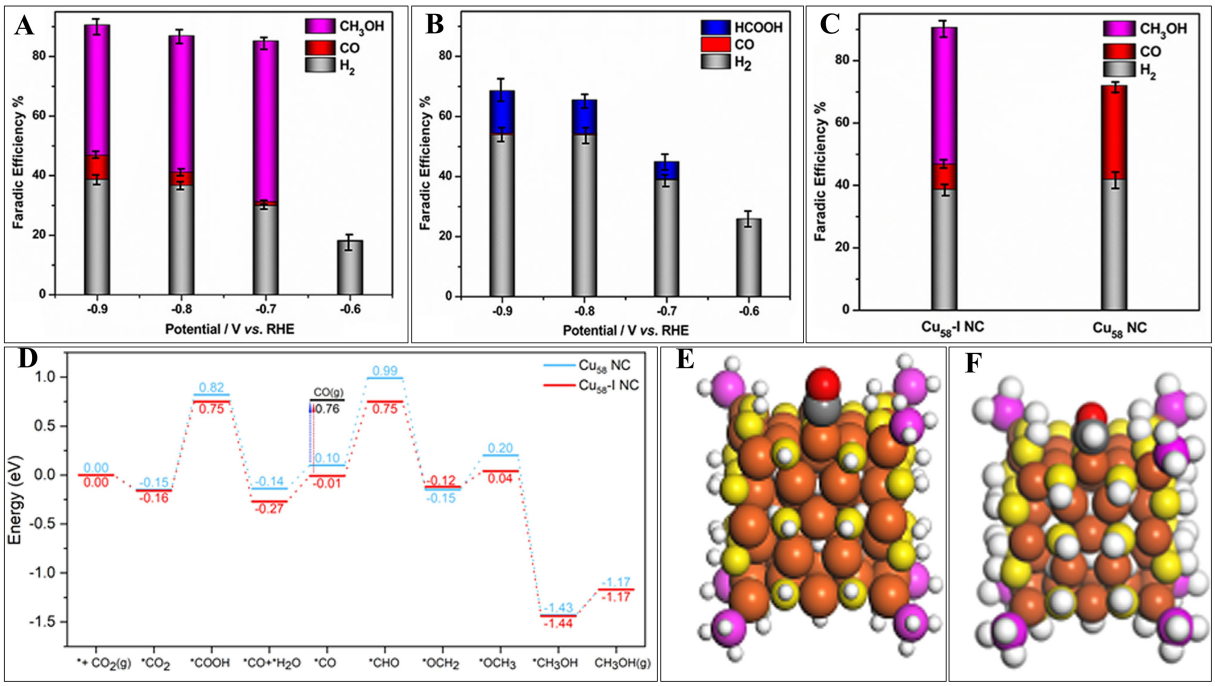

Figure 10. FE of ECO_2RR products for (A) Cu_{58}-I, and (B) Cu_{58}-II; (C) Comparisons of FE for Cu_{58}-1 and Cu_{58} at -0.9 V *vs.* RHE; (D) DFT-based free energy diagram for ECO_2RR on Cu_{58}-I and Cu_{58}; (E) *CO adsorbed on Cu_{58}-1 edge site; (F) *CHO adsorbed on Cu_{58}-1 edge site. Color code: Cu, brown; S, yellow; P, violet; H, white. This figure is reproduced with permission from Ref.[59], Licensed under CC BY 4.0. FE: Faradaic efficiency; RHE: reversible hydrogen electrode; DFT: density functional theory.

methanol on Cu_{58}-1. In contrast, *CO desorption is easier in the case of regular Cu_{58} nanoclusters. Furthermore, the enhanced binding of *CO and *CHO intermediates at the edge Cu site i.e. next to the vertex site with a ligand vacancy in Cu_{58}-I [Figure 10E and F], is attributed to the upshift of d-states of the edge Cu site[59].

Ethanol selective ECO_2RR catalysis: effect of structural transformation

Chen *et al.* synthesized a metastable thiacalix[4]arene-protected $\{NaCu_{35}(TC4A)_4(PhC{\equiv}C)_{20}\}$ (Cu_{35}) cluster shown in Figure 11A[46]. It has a semiring architecture composed of two angularly offset $\{Cu_{17}(TC4A)_2L_9\}$ (L: alkynyl ligand) subunits [Figure 11B], connected by a linear CuL_2 bridging unit [Figure 11C][46]. Each $\{Cu_{17}(TC4A)_2L_9\}$ subunit is composed of two $\{Cu_4$-TC4A$\}$ units linked to $\{Cu_9L_9\}$ core [Figure 11D]. Owing to the structural adaptability of TC4A, Cu_{35} possesses plasticity, resulting in its two distinct occupancy states: one where it coordinates with Na^+ and a second where it encapsulates a CH_2Cl_2 molecule, as shown in Figure 11A. Thus, the central void acts as a potential site for further metal incorporation. Cu_{35} at elevated temperature can undergo fragmentation to form the thermodynamically stable $[Cu_{14}(TC4A)_4(PhC{\equiv}C)_6]$ (Cu_{14}) cluster [Figure 11E]. Further, due to flexibility, a thermal etching of Cu_{35} by Ag^+ can also form bimetallic $[Cu_{14}Ag_6(TC4A)_2(PhC{\equiv}C)_{12}(MeOH)]$ ($Cu_{14}Ag_6$) nanoclusters [Figure 11E]. $Cu_{14}Ag_6$ [Figure 11F] exhibits a dimer composed of two terminal shuttlecock-like $\{Cu_6(TC4A)L_4\}$ units [Figure 11G] and a central $\{Ag_6Cu_2L_4\}$ core [Figure 11H].

All three clusters displayed lower onset overpotentials and enhanced cathodic current densities under CO_2 than under N_2, but their different product distributions represent a clear structural dependence. The monometallic clusters Cu_{14} and Cu_{35} mainly yielded CH_4 and C_2H_4 gas-phase products [Figure 12A and B].

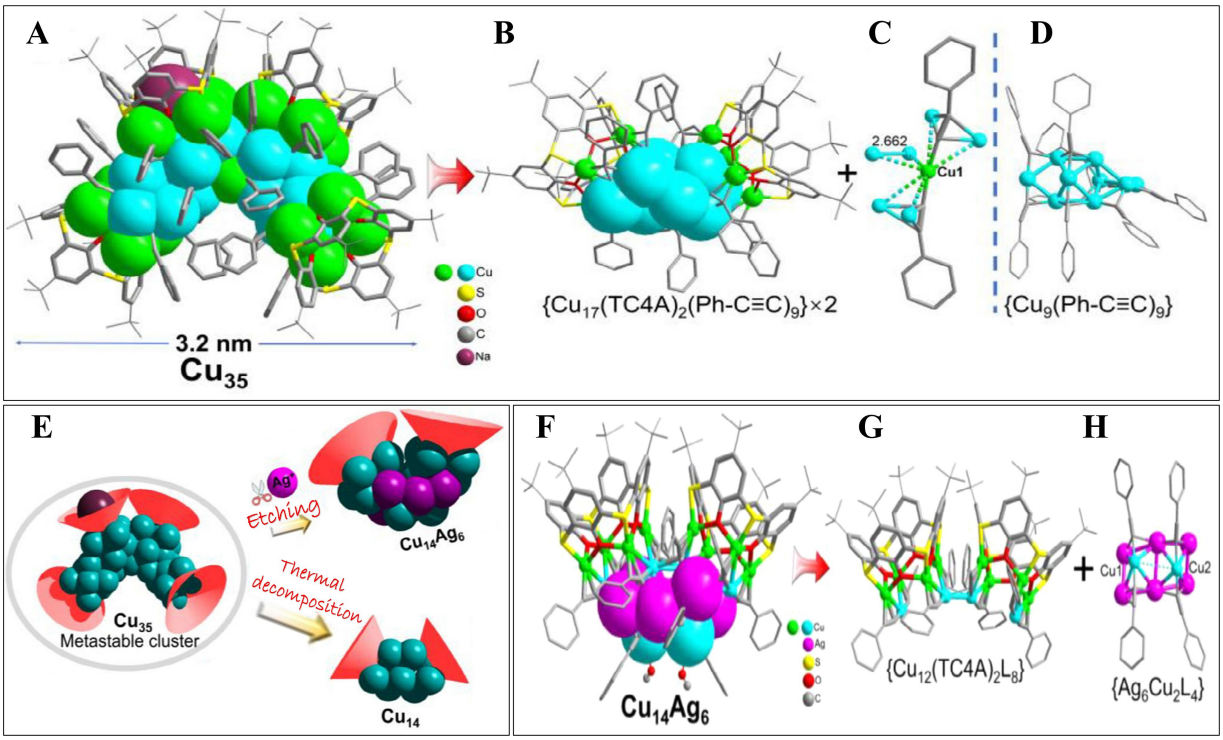

Figure 11. (A) Total crystal structure of Cu_{35}; (B) $\{Cu_{17}(TC4A)_2L_9\}$ subunit; (C) Linear CuL_2 bridging unit; (D) $\{Cu_9L_9\}$ core within Cu_{17} subunit; (E) Two different structural pathways based on metastable Cu_{35}; (F) Structure of $Cu_{14}Ag_6$[46]; (G) The dimer $\{Cu_{12}(TC4A)_2L_8\}$ substructure; (H) The central $\{Ag_6Cu_2L_4\}$ core. This figure is reproduced with permission from Ref.[46], © 2025 Wiley-VCH GmbH.

For instance, Cu_{14} showed a FE_{CH4} ~17.94% and FE_{C2H4} ~27.50% at -1.1 V [Figure 12A]. Similarly, Cu_{35} displays FE_{CH4} ~34.01% and FE_{C2H4} ~13.95% at -1.3 V [Figure 12B]. Notably, monoatomic Cu_{35} and Cu_{14} displayed a limited ethanol selectivity (FE_{C2H5OH} < 7%) across the full potential range. While across the potential range of -0.9 to -1.6 V, $Cu_{14}Ag_6$ exhibits FE_{C2H5OH} > 20% with a maximum FE_{C2H5OH} ~49.27% at -1.3 V [Figure 12C]. Thus, the incorporation of Ag^+ guides the Cu cluster catalysis via stabilizing the key intermediates in the ethanol production pathway. Interestingly, both C_2H_5OH and C_2H_4 routes in ECO_2RR have the same *CO-*COH intermediate. Conventionally, this favors the formation of ethane if it coordinates with two Cu sites through its two carbon atoms. Whereas to obtain ethanol as a selective product, its coordination to a Cu site must be through its oxygen atom rather than its carbon atom [Figure 1].

In $Cu_{14}Ag_6$, the two surface-exposed Cu sites of the Ag_6Cu_2 subunit are the two active sites for ECO_2RR, which have oxyphilic properties that coordinate with CO_2 through the dual-O-bridged adsorption configuration of CO_2, supported by DFT calculations [Figure 12D]. This dual-O-bridged configuration at the two exposed Cu sites undergoes PCET to form bidentate *OCHO, which is further hydrogenated to produce $*OCH_2$ (* represents a Cu site). Simultaneously, at an adjacent Ag site, CO_2 follows conventional C-terminal adsorption and is reduced to #CHO via #COOH (# denotes an Ag site). The intermediates $*OCH_2$ and #CHO formed simultaneously undergo asymmetric coupling to generate $*OCH_2$-CHO, which is further hydrogenated to form CH_3CH_2O* before reduction to ethanol [Figure 12E]. Conversely, Cu---Cu dual sites in Cu_{35} and Cu_{14} favor C_2H_4 formation.

CO selective ECO_2RR catalysts: effect of ligand shells

To discover the effect of complicated multiple surface shells on ECO_2RR, Li *et al.* synthesized $[Cu_{26}(DPPE)_3(CF_3CO_2)_8(CH_3O)_2(^tBuC{\equiv}C)_4H_{11}]^+$ (Cu_{26}) nanocluster, which consists of 26 Cu atoms and five different kinds of ligands such as 1,2-bis(diphenylphosphino)-ethane (DPPE), trifluoroacetate (CF_3COO^-), 3,

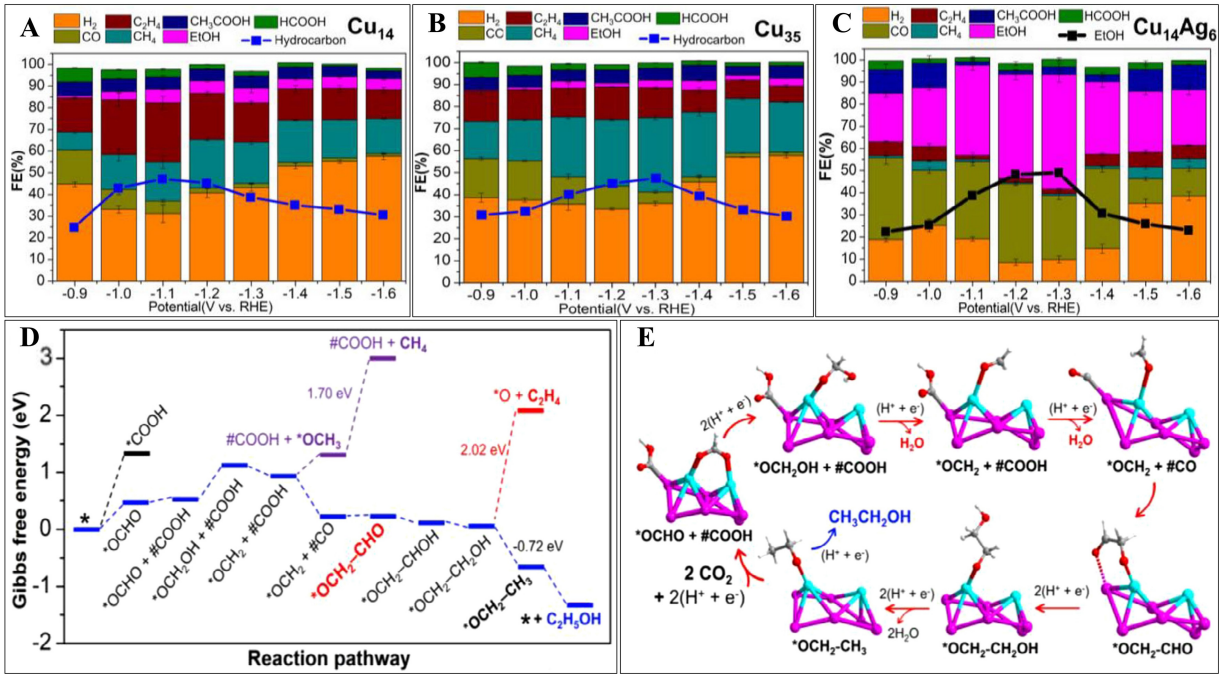

Figure 12. FEs of ECO_2RR products at different applied potentials for (A) Cu_{14}, (B) Cu_{35}, and (C) $Cu_{14}Ag_6$; (D) Free energy profile of ECO_2RR on $Cu_{14}Ag_6$ for ethanol generation; (E) Mechanism for ethanol production by $Cu_{14}Ag_6$ via ECO_2RR. Color code: Cu, cyan; Ag, pink; C, gray; O, red; H, white. This figure is reproduced with permission from Ref.[46], © 2025 Wiley-VCH GmbH. FE: Faradaic efficiency.

3-dimethyl-1-butyne ($^tBuC{\equiv}C^-$), methoxide (CH_3O^-), and hydride ligands[61]. For comparison, other Cu nanoclusters such as $Cu_{25}H_{22}((p\text{-}FPh)_3P)_{12}$ (Cu_{25})[62], $[Cu_{53}(CF_3COO)_{10}(^tBuCC)_{20}Cl_2H_{18}]^+$ (Cu_{53})[63], and $[Cu_{61}(S^tBu)_{26}S_6Cl_6H_{14}]^+$ (Cu_{61})[64] with distinct interfaces were also prepared.

LSV curves suggested that the catalytic activity of CO_2R over different clusters varies substantially [Figure 13A]. The Cu_{26} clusters showed FE_{CO} ~81% at -0.8 V [Figures 13B and C]. But Cu_{53}, in spite of having similar ligands, exhibited much lower FE_{CO} than Cu_{26} at the same potential, indicating the complex surface structure of Cu_{26} created by five ligands favors the formation of CO [Figure 13C]. The plausible reason for the high catalytic efficiency of the Cu_{26} cluster is its strong capability to suppress the competitive HER. Moreover, FE_{H2} for the Cu_{26} was much lower than other clusters under investigation at -0.7 and -0.8 V [Figure 13D]. This suggests that under these potentials, a higher rate of CO_2 adsorption and CO desorption makes CO_2 to CO conversion more prominent on Cu_{26}.

DFT calculations compared the energy barrier for the formation of intermediates for two types of modeled Cu_{26} clusters: Cu_{26} having hydrides and Cu_{26}-H^- (i.e., Cu_{26} without hydrides) [Figure 13E]. Here, the hydrides present in Cu_{26} play an important role in the stabilization of the cluster as well as exposing active sites for selective reduction of CO_2 to CO. However, DFT-based free energy diagrams [Figure 13E and F] revealed that in the absence of hydrides, Cu_{26} clusters can suppress even HER to a great extent and can significantly increase the yield of CO by decreasing the energy barrier for CO* formation.

CO selective ECO_2RR catalysts: role of size and structure

Deng *et al.* synthesized bimetallic nanocluster with composition $[Ag_{15}Cu_6(C{\equiv}CR)_{18}(DPPE)_2]^-$ ($Ag_{15}Cu_6$) [HC≡CR: 3,5-bis(trifluoromethyl)phenylacetylene; DPPE: 1,2-bis(diphenylphosphino)ethane]. $Ag_{15}Cu_6$ exhibits an $Ag_{11}Cu_4$ metal core with a bcc (body-centred cubic) structure capped by two Cu atoms, two Ag_2

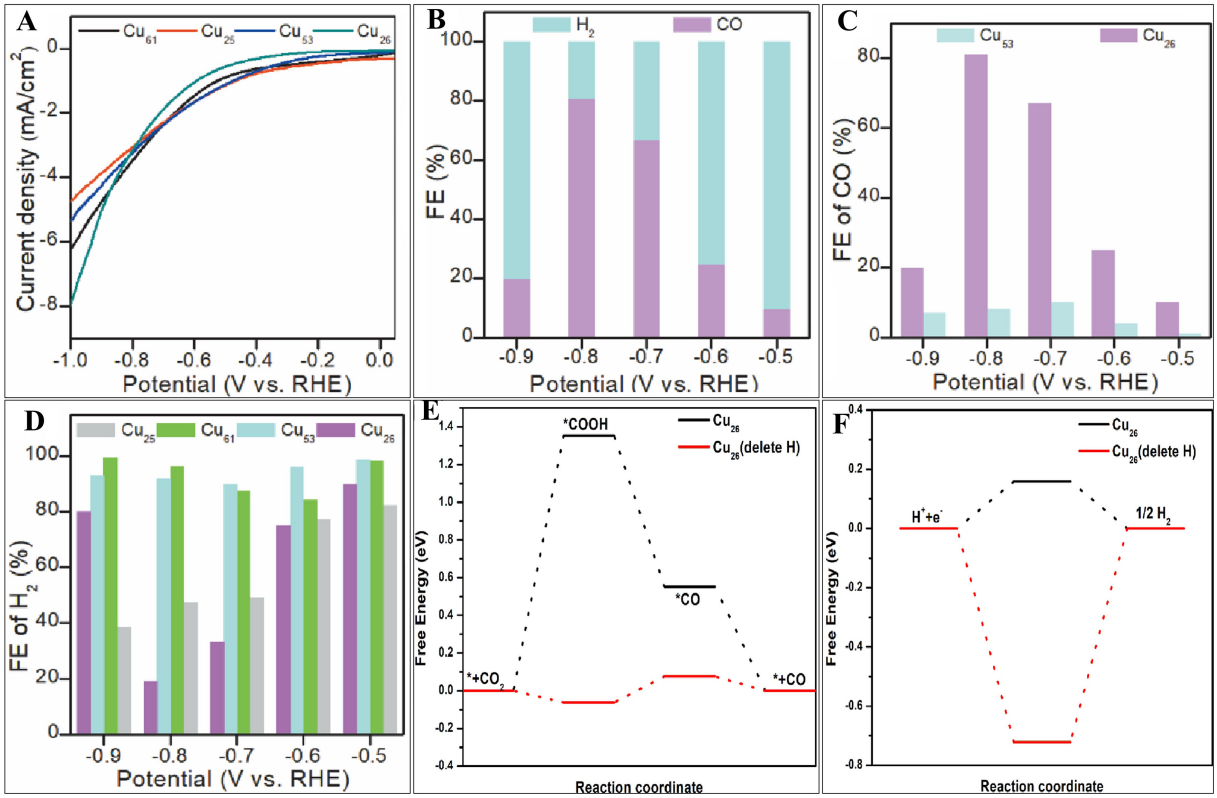

Figure 13. (A) LSV curves of Cu_{26}, Cu_{25}, Cu_{61}, and Cu_{53}; (B) FEs of ECO_2RR products over Cu_{26}; (C) FE_{CO} for Cu_{53} and Cu_{26}; (D) FE_{H2} for Cu_{25}, Cu_{61}, Cu_{53}, and Cu_{26}; (E and F) Free energy diagrams of ECO_2RR and HER pathways on Cu_{26} with and without hydrides (shown by black and red line respectively). This figure is reproduced with permission from Ref.[61], Copyright © 2023 American Chemical Society. LSV: Linear sweep voltammetry; FE: Faradaic efficiency; RHE: reversible hydrogen electrode.

DPPE motifs, and eighteen alkynyl ligands. Such an unusual bcc metal core and accessible surface make it suitable for investigating ECO_2RR[45]. For comparison, the $[Ag_9Cu_6(^tBuC{\equiv}C)_{12}]^+$ (Ag_9Cu_6) cluster possessing a bcc metal core was synthesized. Both these clusters were supported on carbon black ($Ag_{15}Cu_6$/C and Ag_9Cu_6/C) to prevent conductivity problems and enhance dispersion[45]. High current densities in LSV curves were noticed for both the samples in CO_2-saturated solution, indicating their catalytic activity for ECO_2RR[45].

Interestingly, $Ag_{15}Cu_6$/C showed higher current density and lower onset potential than Ag_9Cu_6/C, suggesting the former's higher catalytic activity. The data shown in Figure 14A revealed that $Ag_{15}Cu_6$/C exhibited high selectivity for CO (FE_{CO} > 85%) in the potential range of -0.72 to -0.87 V, with a maximum FE_{CO} ~91.3% at -0.81 V, whereas Ag_9Cu_6/C showed a maximum FE_{CO} ~48.5% at -0.89 V. In a membrane electrode assembly (MEA) electrochemical cell [Figure 14B], $Ag_{15}Cu_6$/C exhibited high selectivity towards CO, with FE_{CO} > 83% at all tested potentials with highest FE_{CO} ~91.3% at -3.50 V and a high partial J_{CO} ~-154 mA·cm^{-2} at -4.00 V. Additionally, $Ag_{15}Cu_6$/C also demonstrated durability as FE_{CO} ~90% and partial current density of ~60 mA·cm^{-2} maintained during 145 h [Figure 14C].

DFT simulations revealed two pairs of AgCu dual metals in $Ag_{15}Cu_6$/C as the most favorable active sites for ECO_2RR owing to the stripping of alkynyl ligands during catalyst preparation without any structural changes, resulting in more available space. Theoretical calculations shown in Figure 14D and E suggested that de-ligated $Ag_{15}Cu_6$ can reduce the exothermic energy barrier of CO_2 to *COOH by 0.21 eV, and the

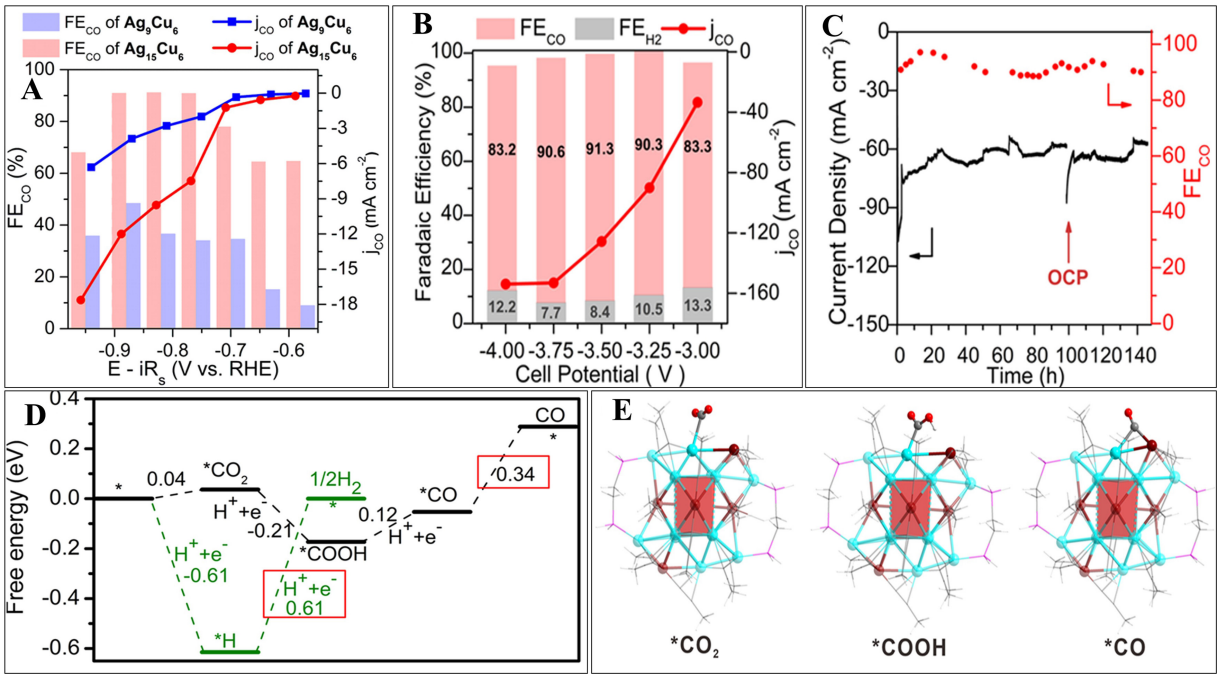

Figure 14. (A) FE_{CO} and j_{CO} for $Ag_{15}Cu_6$/C, and Ag_9Cu_6/C during ECO_2RR; (B) FE_{CO}, FE_{H2}, and j_{CO} of $Ag_{15}Cu_6$/C at various applied potentials in an MEA cell; (C) Long-duration operation of $Ag_{15}Cu_6$/C at -3.25 V in an MEA cell; (D) Free energy diagrams of ECO_2RR and HER on $Ag_{15}Cu_6$ at 0 V (*vs.* RHE) after the removal of a single alkynyl ligand; (E) DFT-based structures of intermediates of $*CO_2$, *COOH, and *CO. Color code: Ag, turquoise; Cu, dark red; P, pink; O, red; C, gray; H, white. This figure is reproduced with permission from Ref.[45], Copyright © 2022 American Chemical Society. MEA: Membrane electrode assembly; HER: hydrogen evolution reaction; RHE: reversible hydrogen electrode; DFT: density functional theory.

desorption of *CO to CO requires overcoming an endothermic energy barrier of 0.34 eV. However, in the competitive reaction pathway of HER, H^+ desorption to form H_2 is a potential-determining step that needs to overcome a large energy barrier of 0.61 V. Thus, it suggested the increase of activity and selectivity of $Ag_{15}Cu_6$ towards CO formation.

Methane selective ECO_2RR catalysis: size effect

Xie *et al.* recently presented tailored Cu nanoclusters to suppress HER while enhancing CO_2 to CH_4 transformation under acidic media[65]. They deposited $[Cu_8(H)(9H\text{-carbazole-9-carbodithiolate})_6]PF_6$ (Cu_8), $[Cu_{36}H_{10}(PET)_{24}(PPh_3)_6Cl_2]$ (Cu_{36}), and $[Cu_{61}(S^tBu)_{26}S_6Cl_6H_{14}]PF_6$ (Cu_{61}) clusters onto carbon paper to make gas diffusion electrodes to test them in a bipolar membrane CO_2RR electrolyzer with an acidic cathode (1 M KCl, pH = 2) and an alkaline anode (1 M KOH). Here, an acidic cathode and basic anode controlled the carbonate formation and minimized ohmic losses to enhance CO_2RR activity. After pre-activation at 200 $mA{\cdot}cm^{-2}$ for 600 s under saturated CO_2, FE_{CH4} for Cu_{36} was found to improve significantly. For instance, Cu_{36} achieved FE_{CH4} ~51.8% ± 1.1% at 300 $mA{\cdot}cm^{-2}$ after activation [Figure 15A], which was higher than FE_{CH4} ~35.3% ± 2% for Cu_{36} without activation. On comparing the ECO_2RR performance of Cu_8, Cu_{36}, and Cu_{61} across the current densities from 200 $mA{\cdot}cm^{-2}$ to 700 $mA{\cdot}cm^{-2}$ using an electrode area of 1.4 cm^2, the striking difference was noticed in their product distribution [Figures 15B-D]. Here, at a current density of 200 $mA{\cdot}cm^{-2}$, the highest selectivity with FE_{CH4} ~35.9% ± 1% was recorded for Cu_{36}, greater than for Cu_8 and Cu_{61}. Whereas, at 200 $mA{\cdot}cm^{-2}$, Cu_8 primarily formed formate (FE_{HCOOH} = 37.7%) with substantial H_2 production (FE_{H2} = 33.9% ± 1%) and minor CH_4 production (FE_{CH4} = 7.0% ± 3.2%) [Figure 15B].

Cu_{61} generated formate (FE_{HCOOH} = 69.4% ± 0.2%) and the lowest CH_4 (FE_{CH4} < 1%) along with H_2 evolution [Figure 15D].

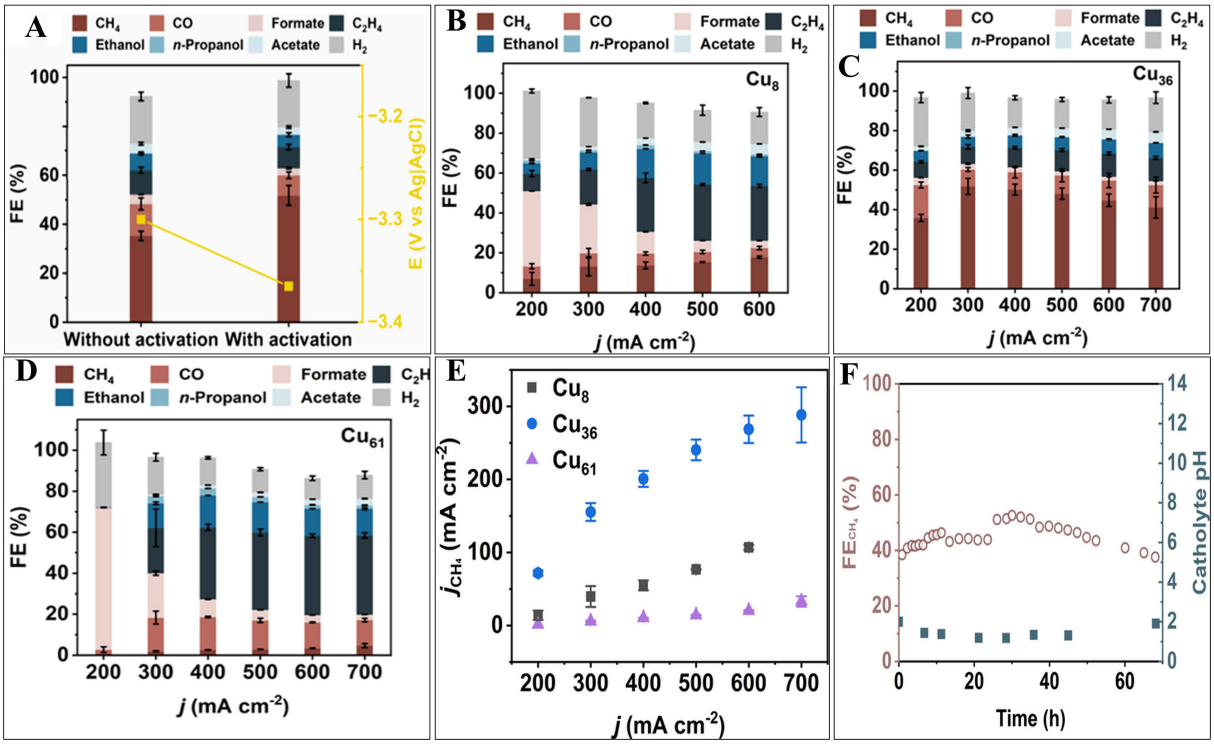

Figure 15. (A) FE of ECO_2RR products at -300 mA·cm^{-2} for Cu_{36}; FE distribution of CO_2RR for (B) Cu_8, (C) Cu_{36}, and (D) Cu_{61} at various current densities; (E) Current density of methane (J_{CH4}) for Cu_8, Cu_{36}, and Cu_{61}; (F) Stability test of Cu_{36} at 300 mA·cm^{-2} in 1 M KCl (pH = 2). This figure is reproduced with permission from Ref.[65], Copyright © 2025 American Chemical Society. FE: Faradaic efficiency.

The stable Cu_{36} maintained the methane selectivity (FE > 40%) across the current density from 300 mA·cm^{-2} to 700 mA·cm^{-2} [Figure 15E]. These results were supported by partial current density (J_{CH4}) curves of Cu_8, Cu_{36}, and Cu_{61} nanoclusters. In contrast to Cu_{36}, an explicit transition in product distribution was observed from C_1 to C_{2+} for Cu_8 and Cu_{61} across the 200 mA·cm^{-2} to 700 mA·cm^{-2} [Figure 15B-D][65]. Here, C-C coupling reactions responsible for C_2H_4 and C_2H_5OH formation were due to nanocluster aggregation owing to instability of thiolate ligands on Cu_8 and Cu_{61} at high current densities, resulting in the formation of crystalline $Cu_{2-x}S$ nanoparticles creating more favorable active sites to generate C_2 products. However, in case of Cu_{36}, the thiolate ligands prevented such agglomeration. The Cu_{36} also maintained constant activity and selectivity for 70 h at -300 mA·cm^{-2} [Figure 15F].

In another report, Han *et al.* demonstrated size effects on ECO_2RR for $[Cu_{13}(SC_6H_3F_2)_3(P(PhF)_3)_7H_{10}]$ (Cu_{13}) and $[Cu_{14}(SC_6H_3F_2)_3(P(PhF)_3)_8H_{10}]^+$ (Cu_{14}) nanoclusters with precise structures shown in Figure 16A and B, where even one atom alteration results in switching of catalytic reactivity[66]. Here, Cu_{14} has a $Cu(PR_3)$ vertex at its defect site [Figure 16C], and this additional Cu atom at the top of Cu_{14} allows the H atom bound to three core Cu atoms to move into the center of the same Cu_3 plane. As a result, the electronic structure of surrounding atoms is tuned to facilitate the CO_2 adsorption and H_2O dissociation simultaneously on Cu_{14}.

For Cu_{13}, H_2 was the main product with little CO across the whole potential range of -0.8 to -1.3 V [Figure 17A]. Notably, for Cu_{14}, with an increase of applied voltage from -0.8 to -1.2 V, FE_{CO} gradually decreases from 43% to 10.3%, while $FE_{CH4+C2H4}$ was found to be ~54.3% at -1.2 V with a corresponding current density of carbon-containing products ($J_{carbon\ containing\ products}$) of 60 mA·cm^{-2} [Figure 17B]. Upon a further increase of potential to -1.3 V, H_2 evolution becomes extreme, resulting in a significant decrease in CO_2RR activity of Cu_{14}. It is worth noting here that the decreasing trend of FE_{CO} and increasing trend of FE of

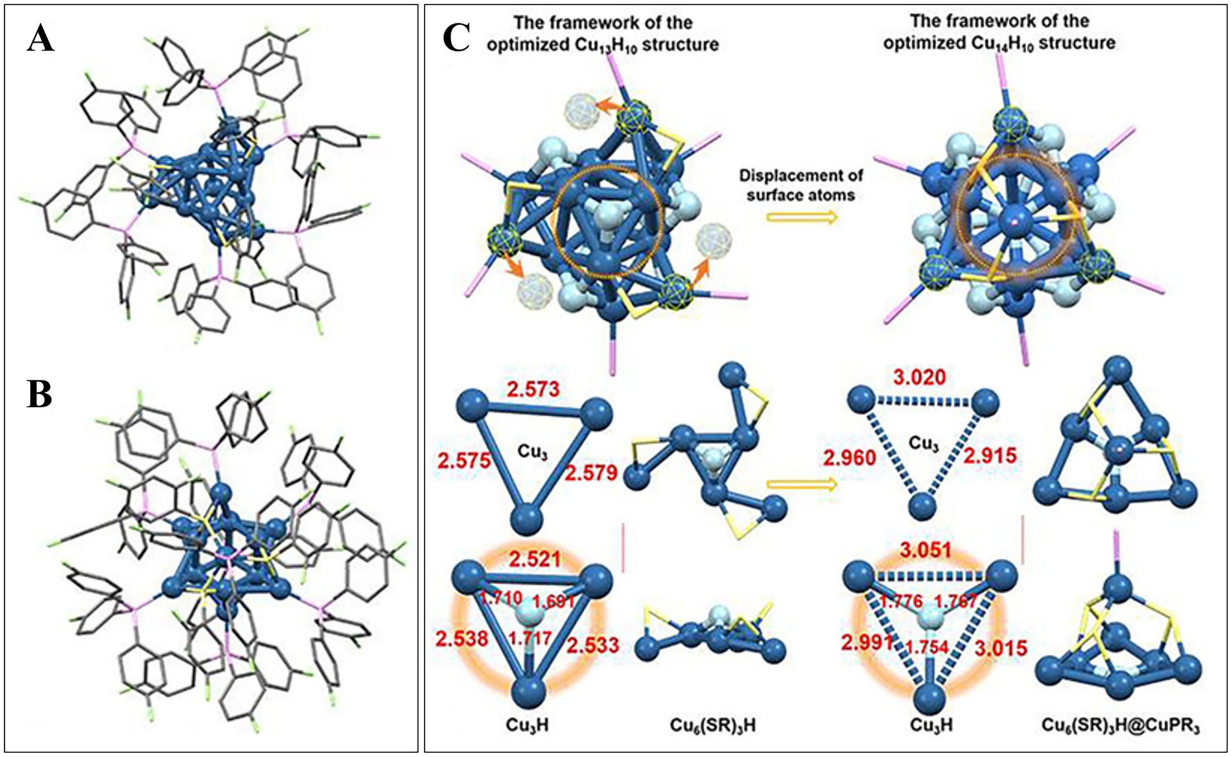

Figure 16. Total structures of (A) Cu_{13} and (B) Cu_{14}; (C) Structural comparisons between Cu_{13} and Cu_{14}. Color code: Cu, blue; H, cyan. This figure is reproduced with permission from Ref.[66], © 2025 Wiley-VCH GmbH.

carbon-containing hydrocarbons in the potential range of -0.8 to -1.2 V indicate that CO_2 to CH_4 and C_2H_4 conversion occurs via a *CO intermediate. Interestingly, an increase in the rate of formation of carbon-containing products with an increase in pH indicates that Cu_{14} speeds up H_2O activation even at higher pH[66].

Furthermore, *in situ* FTIR (Fourier transform infrared spectroscopy) monitoring revealed that the *CO peak in Cu_{14} becomes more intense with time, suggesting accumulation of *CO on Cu_{14} leading to further deep hydrogenation[66]. Next, Gibbs free energy calculations showed that the formation of the *COOH intermediate was more favorable in the case of Cu_{14} (ΔG = 0.39 eV) than in Cu_{13} (ΔG = 0.91 eV) [Figure 17C]. ΔG curves further indicate that H_2O dissociation is also more feasible on Cu_{14} than on Cu_{13} [Figure 17D]. But the *CO desorption on Cu_{14} was found more difficult (ΔG = 1.15 eV), which promoted its deep hydrogenation to produce hydrocarbons [Figure 17E and F].

Methane and ethylene selective ECO_2RR catalysis: effect of coordination symmetry of metal active site

The coordination symmetry breaking of the metal center results in an increase in active sites. Wu *et al.* demonstrated this kind of breaking of coordination symmetry in thiolate-protected $Cu_6(MBD)_6$ (MBD: 2-mercaptobenzimidazole) nanoclusters having symmetry-broken CuS_2N_1 active sites and its impact on ECO_2RR[58]. The $Cu_6(MBD)_6$ displayed a maximum current density of ~364 mA·cm^{-2} at -1.5 V in saturated CO_2 [Figure 18A]. The product distribution analysis shown in Figure 18B revealed that at an applied potential of +0.7 V, CO was the main product (FE_{CO} > 31.8%) along with CH_4 (FE_{CH4} ~2.1%) and C_2H_4 (FE_{C2H4} ~3.5%). However, with an increase in applied potential, FE_{CO} gradually decreased, while FE_{CH4} and FE_{C2H4} continuously increased till FE_{CH4} reached 42.5% at -1.4 V (J_{CH4} = -119 mA·cm^{-2}), along with FE_{C2H4} reaching 23% (J_{C2H4} = -64.4 mA·cm^{-2}) [Figure 18C].

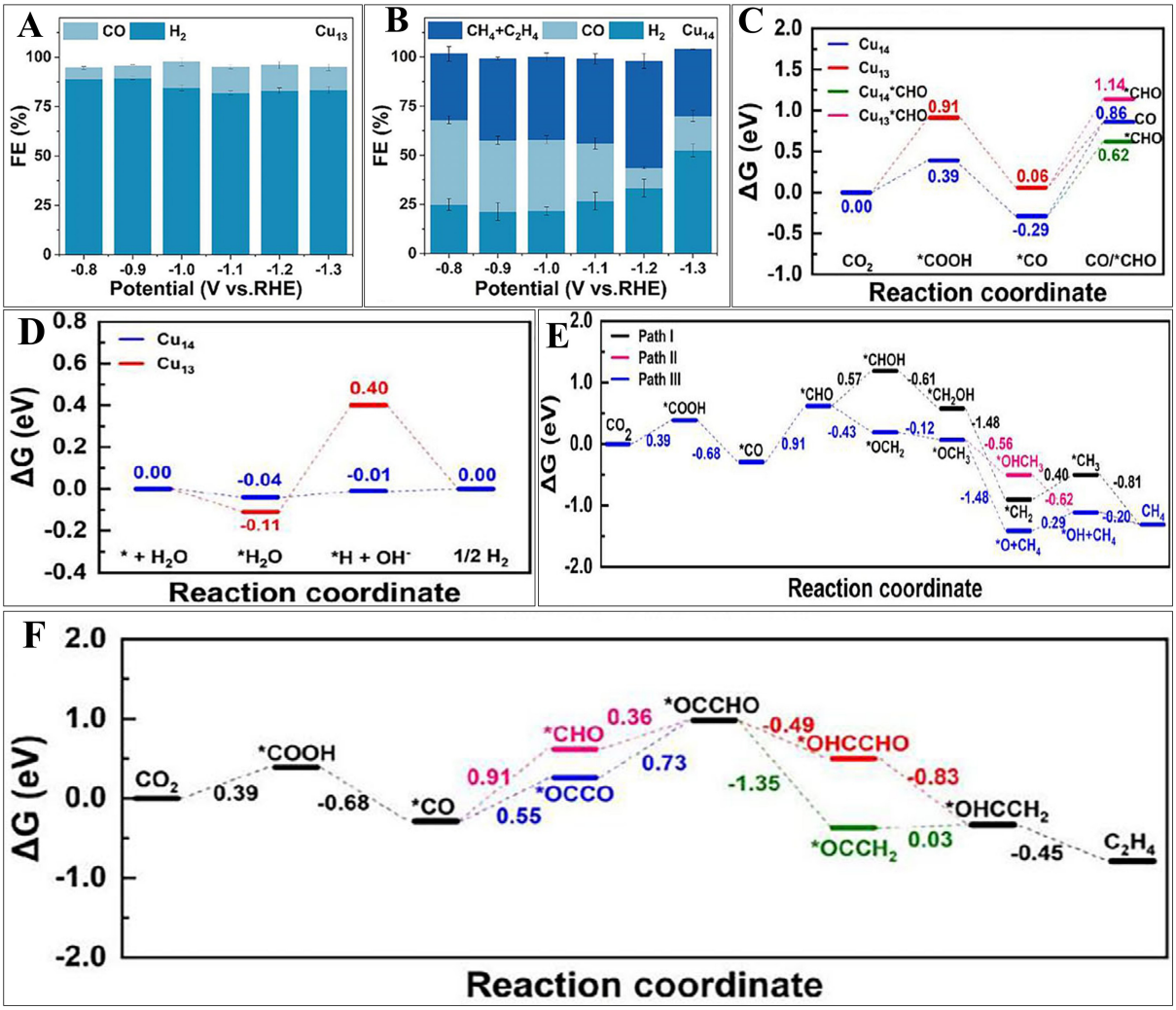

Figure 17. FE of products in ECO_2RR over (A) Cu_{13} and (B) Cu_{14}; ΔG curves for (C) reduction of CO_2 to CO/*CHO, (D) H_2O dissociation, (E) CH_4 formation, and (F) C_2H_4 formation on Cu_{14} and Cu_{13}. This figure is reproduced with permission from Ref.[66], © 2025 Wiley-VCH GmbH. FE: Faradaic efficiency.

Further, DFT calculations were performed using optimized geometric models of $Cu_6(MBD)_6$ with CuS_2N_1 active sites and $Cu_8(^tBuS)_4(L2)_4$ (L2: o-ethyl carbonodithiolate) with Cu-S_3 sites. Unlike in $Cu_8(^tBuS)_4(L2)_4$, electron transfer from $Cu_6(MBD)_6$ to CO_2 was noticed owing to the higher polarity of the Cu-S_2N1 site relative to the Cu-S_3 site [Figure 18D], and the higher binding energy (0.19 eV) between $Cu_6(MBD)_6$ and CO_2 than between CO_2 and $Cu_8(^tBuS)_4(L2)_4$ (0.18 eV). Integrated projected density of states (IPDOS) revealed that for $Cu_6(MBD)_6$, the d_{x2-y2} orbital of the CuS_2N_1 site is the highest occupied d-orbital [Figure 18E], and for $Cu_8(^tBuS)_4(L2)_4$, the d_{xz} of the CuS_3 site is the highest occupied d-orbital [Figure 18F]. Further, for $Cu_6(MBD)_6$, the symmetry and energy match of its highest occupied d_{x2-y2} orbital with the lowest occupied π* orbital of CO_2 to form a π-complex via π-back bonding plays a role in binding the reactant and intermediate [Figure 18G]. In contrast, the highest occupied d_{xz} orbital of $Cu_8(^tBuS)_4(L2)_4$ would couple with the lowest occupied π* orbital of CO_2 to form a π-complex only when the adsorption of CO_2 occurs through the O atom [Figure 18H]. The key intermediate in the case of $Cu_6(MBD)_6$, was *COOH instead of *OCHO. On the basis of adsorption free energies of key intermediates at an applied potential of -1.4 V shown in Figure 18I, the CuS_2N_1 adsorbs the CO_2 with a free energy of -0.13 eV, leading to their strong interaction followed by hydrogenation through adding a proton and electron from the electrode to form the *COOH intermediate.

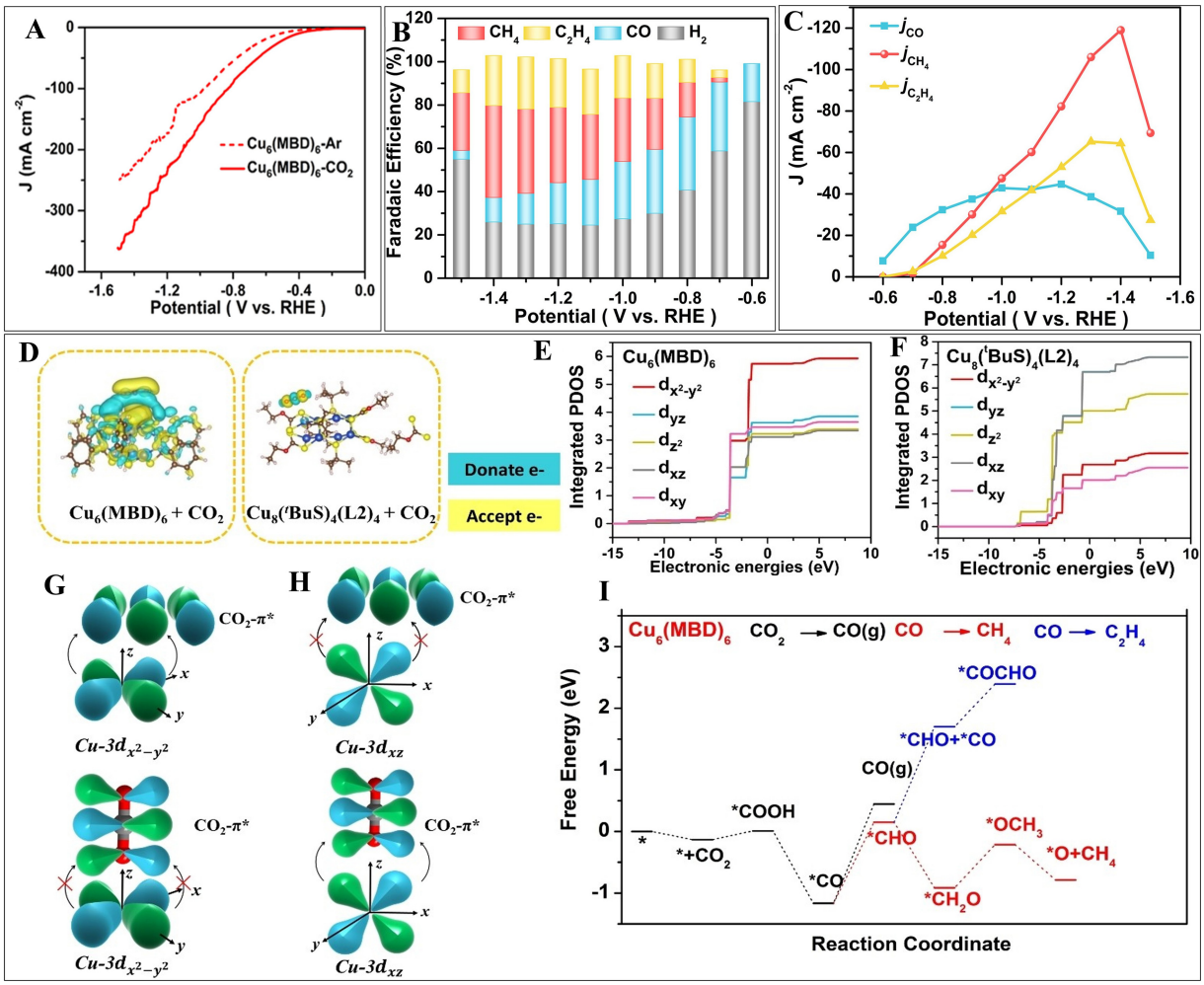

Figure 18. (A) LSV curves of $Cu_6(MBD)_6$ under saturated CO and Ar; (B) FEs of ECO_2RR products (CH_4, C_2H_4, and CO) at different applied potentials for $Cu_6(MBD)_6$; (C) Current densities of ECO_2RR products on $Cu_6(MBD)_6$; (D) Charge density contrast plots at $Cu_6(MBD)_6/CO_2$ and $Cu_8(^tBuS)4(L2)_4/CO_2$ interface; Density of states relative to Fermi level on Cu atom in (E) $Cu_6(MBD)_6$ and (F) $Cu_8(^tBuS)_4(L2)_4$; Different modes of CO_2 binding with Cu sites considering d_{x2-y2} and d_{xz} as highest occupied d orbitals in (G) $Cu_6(MBD)_6$ and (H) $Cu_8(^tBuS)_4(L2)_4$, respectively; (I) Free energy diagram of CO_2RR on $Cu_6(MBD)_6$ at -1.4 V. This figure is reproduced with permission from Ref.[58], © 2023 Wiley-VCH GmbH. RHE: Reversible hydrogen electrode.

This is followed by generation of *CO, which can either undergo desorption or hydrogenation to form CH_4 and/or C_2H_4 as products.

Methane selective ECO_2RR catalysis: synergic effect of dual sites

Li *et al.* illustrated the impact of the synergistic effect of dual sites, such as Cu^+ and adjacent S sites, on ECO_2RR. To this end, they synthesised $Cu_4(MMI)_4$ (Cu_4) and $Cu_8(MMI)_4(^tBuS)_4$ (Cu_8) (MMI: 2-mercapto-1-methylimidazole) nanoclusters with well-resolved structures as shown in Figure 19A and B, respectively[67]. LSV curves of both Cu_4 and Cu_8 exhibited high current densities in saturated CO_2, confirming their high activities for ECO_2RR. Cu_4 exhibited FE of carbon products > 85.8% across the potential from -0.9 to -1.6 V with a maximum FE ~94.0% at -1.2 V [Figure 19C]. The carbonaceous hydrocarbons formed on Cu_4 via ECO_2RR were CH_4 (FE_{CH4} ~53.7%), C_{2+} products (FE_{C2+} ~37.3%), and CO and HCOOH ($FE_{CO+HCOOH}$ < 8.2%) at -1.2 V. This indicates that the Cu(I) site in Cu_4 effectively stabilizes the *CO, which is further reduced into high-value carbonaceous products. In contrast, FE of deep-reduced carbonaceous products for Cu_8 was found to be ~72.8% at -1.2 V [Figure 19D], along with FE of 2e-reduction products ~15.8% and FE_{H2} ~11.4%. Notably, Cu_4 showed a high preference for CH_4 with FE_{CH4} ~53.7% and J_{CH4} ~89.1 mA·cm^{-2} at -1.2 V (*vs.*

RHE), whereas Cu_8 exhibits a preference for C_{2+} products with FE ~58.5% and J_{C2+} of 152.1 mA·cm^{-2} at -1.3 V (*vs.* RHE)[67]. Interestingly, the continuous electrolysis revealed higher electrochemical stability of Cu_4.

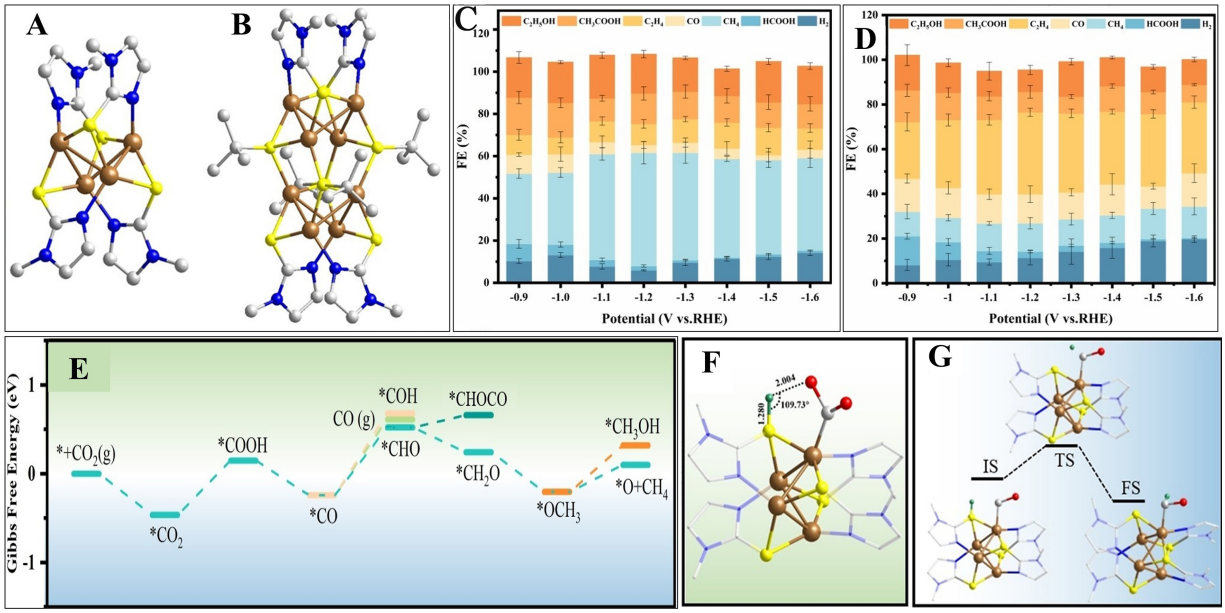

Figure 19. Total structure of (A) Cu_4 and (B) Cu_8; FE of CO_2RR products on (C) Cu_4 and (D) Cu_8; (E) Free energy diagram of CO_2RR on Cu_4.; (F) Mechanism of hydrogen bond interaction between *H and reaction intermediates; (G) Relative free energies of initial configuration (IS), transition states (TS), and final configuration (FS) for *CO protonation to *CHO. This figure is reproduced with permission from Ref.[67], © 2024 Wiley-VCH GmbH. RHE: Reversible hydrogen electrode; FE: Faradaic efficiency.

Further, ATR-SEIRAS analysis displayed the peaks corresponding to the OH deformation and symmetric stretch of *COOH, which is key intermediate to form CO and CH_4 products in case of Cu_4[67]. Furthermore, the peaks of *CH_2O and *OCH_3, which are crucial intermediates to form CH_4, were also noticed. Although most of the reaction intermediates on Cu_4 are similar to Cu_8, the appearance of peaks corresponding to the *COCHO intermediate indicates the formation of C_{2+} products in Cu_8. The Gibbs free energy diagram for Cu_4, shown in Figure 19E, revealed that the C-C coupling step of *CHOCO is uphill, with a barrier of 0.19 eV inhibiting the production of multicarbon products. Furthermore, the Gibbs formation energy of *CH_3OH from the *OCH_3 intermediate is 0.22 eV higher than that of CH_4 for Cu_4. The proposed mechanism of hydrogen bond interaction between H* and reaction intermediate is presented in Figure 19F along with relative free energies of initial configuration, transition state, and final configuration for protonation of *CO to *CHO [Figure 19G]. On the other hand, taking into account experimental findings that one tert-butyl group is removed, the energy barrier for *COCHO formation is lower than *CHO protonation on both CuS_2N and Cu-S_3 sites, indicating a stronger tendency of Cu_8 to form C_{2+} products.

The Faradaic efficiencies of products formed during ECO_2RR over various ligand-protected Cu nanoclusters mentioned in this review are summarized in Table 1.

PHOTOCATALYTIC CO_2 REDUCTION REACTIONS (PCO_2RR)

Fundamental principle

The photocatalytic CO_2 reduction under a continuous solar spectrum performs like artificial photosynthesis, which involves three typical processes: (i) charge carrier (electron-hole pair) formation upon light absorption; (ii) charge carrier separation and transport; and (iii) surface redox reactions. For efficient surface reactions, the charge recombination rate must be slower than the rate of charge transfer to chemical species.

Table 1. Summary of Cu nanocluster-based ECO_2RR catalysis along with FE of products

Cu nanocluster-based electrocatalysts	Potential	Faradaic efficiency (FE) of products	Reactor	Ref.
$[Cu_{32}(H)_{20}\{S_2P(O^iPr)_2\}_{12}]$ (Cu32) W.E.: Cu_{32}/CB/GDL (1 cm^2) Electrolyte: 0.1 M $KHCO_3$ + 0.4 M KCl, pH ~6.8	0.3 V overpotential	FE_{HCOOH} ≈89%; minor products: CO and H_2; TON ~1740 for 90 min	H-cell	[54]
$[Cu_{14}(CHT)_3(PPh_3)H_{10}]^+$ (Cu_{14}-CHT) W.E.: Cu_{14}-CHT/CB/carbon paper Electrolyte: 0.1 M $KHCO_3$, pH~7	-1.2 V	FE_{HCOOH} ≈31%; FE_{CO} ≈8%; For 12 h, consistent FE_{HCOOH} ≈12 %; other product = H_2	Flow-cell	[55]
$[Cu_{14}(PET)_3(PPh_3)_8H_{10}]^+$ (Cu_{14}-PET) W.E.: Cu_{14}-PET/CB/carbon paper Electrolyte: 0.1 M $KHCO_3$, pH ~7	-1.2 V	FE_{HCOOH} ≈39%; FE_{CO} ≈2%; For 12 h, consistent FE_{HCOOH} ≈35%; other product = H_2	Flow-cell	[55]
$Cu_8(H)(L1)_6PF_6$ (Cu_8-1), (cubic kernel) W.E.: Cu_8-1/C/carbon fiber cloth Electrolyte: 0.5 M $KHCO_3$	-1.0 V	FE_{HCOOH} ≈48.6%; FE_{CO} < 5%; FE_{H2} ~40%)	H-cell	[56]
$Cu_8(^tBuS)_4(L1)_4$ (Cu_8-2), (ditetrahedral kernel) W.E.: Cu_8-2/C/ carbon fiber cloth Electrolyte: 0.5 M $KHCO_3$	-1.0 V	FE_{HCOOH} ≈92%; FE_{CO} ~10%; FE_{H2} < 5%	H-cell	[56]
$[Cu_{23}H_4(SC_7H_7)_{18}(PPh_3)_6]$ (Cu_{23}) W.E.: Cu_{23}/CB/carbon paper Electrolyte: 0.5 M $KHCO_3$	-1.2 V	FE_{HCOOH} ≈26%; FE_{H2} ≈43%; other minor product: CO; TOF for HCOOH~113.4 h^{-1}	H-cell	[43]
$[Cu_{17}H_6(NHC^H)_4(dppm)_4]^{3+}$ (Cu17a) W.E.: Cu17a/CNT/GDC Electrolyte: 1 M KOH	-0.37 V -1.07 V	FE_{CO} ≈91%; FE_{H2} < 10% FE_{C2H4} ≈37.5%; FE_{CO} < 35%; FE_{H2} < 30%	Flow-cell	[57]
$[Cu_{17}H_6(NHC^{ph})_4(dppm)_4]^{3+}$ (Cu17b) W.E.: Cu17b/CNT/GDC Electrolyte: 1 M KOH	-0.6 - 0.8 V	FE_{CO} ≈36%; other product = H_2	Flow-cell	[57]
$[Cu_{58}H_{20}(SPr)_{36}(PPh_3)_7]^{2+}$ (Cu_{58}-1) W.E.: Cu_{58}-1/CB/carbon paper Electrolyte: 0.1 M $KHCO_3$	-0.7 V	FE_{CH3OH} ≈54%; FE_{H2} < 30%; minor product: CO	H-cell	[59]
$[Cu_{58}H_{20}(SEt)_{36}(PPh_3)_6]^{2+}$ (Cu_{58}-II) W.E.: Cu_{58}-II/CB/carbon paper Electrolyte: 0.1 M $KHCO_3$	-0.9 V	FE_{H2} > 50%; FE_{HCOOH} ~15%; minor product: CO	H-cell	[59]
$[Cu_{58}H_{20}(SPr)_{36}(PPh_3)_7]^{2+}$ (Cu_{58}) W.E. : Cu_{58}/CB/carbon paper Electrolyte: 0.1 M $KHCO_3$	-0.9 V	FE_{CO} ≈30%; FE_{H2} ~40%	H-cell	[59]
$\{NaCu_{35}(TC_4A)_4(PhCC)_{20}\}$ (Cu_{35}) W.E: Cu_{35}/CNT/carbon paper Electrolyte: 1 M KOH	-1.3 V	FE_{CH4} ≈34.01%; FE_{C2H4} ≈13.95%; FE_{CO} ~5%; FE_{H2} ~37%; FE_{C2H5OH} < 5%	Flow-cell	[46]
$[Cu_{14}(TC_4A)_4(PhCC)_6]$ (Cu_{14}) W.E: Cu_{14}/CNT/carbon paper Electrolyte: 1 M KOH	-1.1 V	FE_{CH4} ≈17.94%; FE_{C2H4} ≈27.50%; FE_{H2} ~30%; FE_{CO} ~5%; FE_{C2H5OH} < 7%	Flow-cell	[46]
$[Cu_{14}Ag_6(TC_4A)_2(PhC{\equiv}C)_{12}(MeOH)]$ ($Cu_{14}Ag_6$) W.E.: $Cu_{14}Ag_6$/CNT/carbon paper) Electrolyte: 1 M KOH	-1.3 V	FE_{EtOH} ~49.27%; FE_{CO} ~30%; FE_{C2H4} ~1.87%; FE_{H2} < 10%	Flow-cell	[46]
$[Cu_{26}(DPPE)_3(CF_3CO_2)_8(CH_3O)_2(^tBuC{\equiv}C)_4H_{11}]^+$ (Cu_{26}) W.E: Cu_{26}/CB/carbon paper Electrolyte: 0.1 M $KHCO_3$ + 0.4 M KCl	-0.8 V	FE_{CO} ≈81%; other products = H_2	H-cell	[61]
$[Ag_{15}Cu_6(C{\equiv}CR)_{18}(DPPE)_2]^-$ ($Ag_{15}Cu_6$) W.E.: $Ag_{15}Cu_6$/C/carbon paper Electrolyte: 0.1 M $KHCO_3$	-0.81 V	FE_{CO} ≈91.3%; FE_{H2} ≈7%	H-cell	[45]
$[Ag_9Cu_6(^tBuC{\equiv}C)_{12}]^+$ (Ag_9Cu_6) W.E.: Ag_9Cu_6/C/carbon paper Electrolyte: 0.1M $KHCO_3$	-0.89 V	FE_{CO} ≈48.5%; other product: H_2	H-cell	[45]
$[Cu_8(H)(9H\text{-carbazole-9-carbodithiolate})_6]PF_6$ (Cu_8) W.E: Cu_8/carbon substrate) Electrolyte: catholyte 1 M KCl, pH = 2 and anolyte 1 M KOH	@ 200 mA·cm^{-2}	FE_{HCOOH} ~37.7%; FE_{C2+} ≈16.2% 2%; FE_{H2} ≈33.9% 1.0%; FE_{CH4} ≈7.0%)	Flow-cell	[65]
$[Cu_{36}H_{10}(PET)_{24}(PPh_3)6Cl_2]$ (Cu_{36}) W.E.: Cu_{36}/carbon substrate Electrolyte: catholyte 1M KCl, pH = 2 and anolyte 1 M KOH	@ 200 mA·cm^{-2}	FE_{CH4}=35.9 1.8%; other products: CO, C_2H_4, C_2H_5OH, HCOOH, CH_3COOH, and H_2	Flow-cell	[65]

$[Cu_{61}(S^tBu)_{26}S_6Cl_6H_{14}]PF_6$ (Cu_{61}) W.E.: Cu_{61}/carbon substrate Electrolyte: catholyte 1 M KCl, pH = 2 and anolyte 1 M KOH	@ 200 mA·cm^{-2}	FE_{HCOOH} ≈69.4% ± 0.2%; FE_{CH4} < 1%; FE_{H2} ~33%	Flow-cell	[65]
$[Cu_{13}(SC_6H_3F_2)_3(P(PhF)_3)_7H_{10}]^0$ (Cu_{13}) W.E.: Cu_{13}/caron fiber paper Electrolyte: 0.5 M $KHCO_3$	-1.1 V	FE_{CO} ≈13%; FE_{H2} ≈85%	H-cell	[66]
$[Cu_{14}(SC_6H_3F2)_3(P(PhF)_3)_8H_{10}]^+$ (Cu_{14}) W.E.: Cu_{14}/caron fiber paper Electrolyte: 0.5 M $KHCO_3$	-1.2 V	$FE_{CH4+C2H4}$ ≈54.3% ; FE_{CO} ≈10.3% ; other product: H_2	H-cell	[66]
$[Cu_6(MBD)_6]$ ($Cu_6(MBD)_6$) W.E.: $Cu_6(MBD)_6$/carbon paper Electrolyte: 1 M KOH	-0.7 V -1.4 V	FE_{CO} ≈31.8%; minor products: CH_4 and C_2H_4 FE_{CH4} ≈42.5%; FE_{C2H4} ≈23; minor product: CO	Flow cell	[58]
$Cu_4(MMI)_4$ (Cu_4) W.E.: Cu_4/carbon paper Electrolyte: 1 M KOH	-1.2 V	FE_{CH4} ≈53.7%; FE_{C2+} ≈37.3%; other minor products: CO, H_2. HCOOH, CH_3COOH	Flow cell	[67]
$Cu_8(MMI)_4(^tBuS)_4$ (Cu_8) W.E.: Cu_8/carbon paper Electrolyte: 1 M KOH	-1.3 V	FEC_{2+} ≈58.5%; FE_{C1}≈15.8%; FE_{H2} ≈11.4%	Flow cell	[67]

W.E.: Working electrode; CHT: cyclohexane thiolate; PET: 2-phenylethane thiolate; L1: 9H-carbazole-9-carbodithiol; NHC^{H}: 1,3-diprop-2-ynyl-1H-imidazol-3-ium hexafluorophosphate ($H_3NHCH{\cdot}PF_6$); NHC^{Ph}: 1,3-bis(2-propyn-1-yl)-1H-benzoimidazol-3-ium hexafluorophosphate ($H_3NHCPh{\cdot}PF_6$); dppm: bis(diphenylphosphino)methane; TC_4A: thiacalixarene[4]arene; DPPE: 1,2-bis(diphenylphosphino)ethane; MBD: 2-mercaptobenzimidazole; MMI: 2-mercapto-1-methylimidazole.

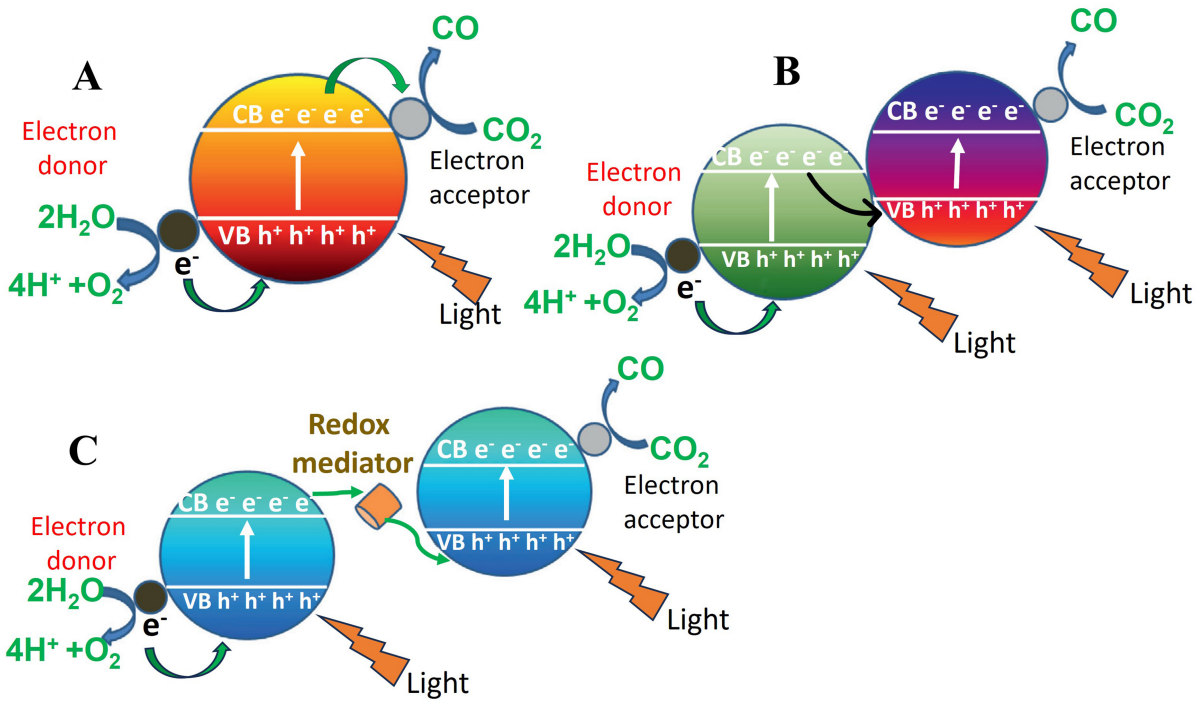

Figure 20. Photocatalytic systems: (A) Single excitation photosystem with a wide band gap; (B) Multiple excitation system with a pair of narrow band gap photocatalysts connected with a heterojunction; (C) Multiple excitation system connected with an electron mediator to form a Z scheme. This figure is reproduced with permission from Ref.[68], © 2021 Elsevier B.V. All rights reserved.

Thermodynamically, the conduction band position of the photocatalyst should be more negative than the reduction potential of CO_2 (~-0.48 V *vs.* RHE, pH = 7), while the valence band should be at a more positive potential than the oxidation potential of water (+0.81 to +0.82 V *vs.* RHE, pH = 7). Artificial photocatalytic systems are mainly of three kinds [Figure 20A-C][68]: (1) single excitation system with a wide band gap photocatalyst; (2) multiple excitation system with a pair of narrow band gap materials coupled with each other via a physical contact (heterojunction); (3) multiple excitation systems connected by a redox mediator to form a Z scheme.

The reported examples of Cu nanoclusters as photocatalysts are relatively few and are illustrated in the following section.

Ligand-protected Cu nanocluster for PCO_2RR

CO selective PCO_2RR: ligand effect

The S, N atom-based coordination compounds are in more negative p-orbitals (lower in energy) relative to O atoms and can be coupled to produce more desirable band structures. With this understanding, Dong *et al.* synthesized $Cu_6(HL_1)_2(L_1)_4(PF_6)_2$ (Cu_6-NH), (L_1 = PymSH = 2-mercaptopyrimidine) nanocluster[69]. The Cu_6-NH exhibited a distorted Cu_6 octahedron with 6 faces capped by six ligands with alternate alignment, as shown in Figure 21A. Interestingly, the two N atoms in Cu_6-NH are protonated to balance the two PF_6^- counterions [Figure 21B], which is contrary to Cu_6-N [Figures 21C and D], where all ligands are fully deprotonated. Structural analysis showed an identical metal core for both Cu_6-NH and Cu_6-N [Figure 21E]. The strong hydrogen-bonded network among clusters and between clusters and PF_6^- forms a stacking network in Cu_6-NH [Figure 21F] compared to weaker intermolecular interactions seen in Cu_6-N [Figure 21G].

UV-Vis (ultraviolet-visible) spectra indicated that Cu_6-NH and Cu_6-N have absorption in 400-550 nm. The conduction bands of both clusters were more negative (-1.08 and -1.11 V, respectively) than the redox potential of CO/CO_2 (-0.48 V, pH = 7), and the valence bands of both clusters are more positive than the redox potential of O/H_2O (+0.82 V, pH = 7), indicating both can catalyze CO_2 reduction and H_2O oxidation. DFT calculations revealed that both nanoclusters are direct band gap semiconductors with p-n heterostructures for efficient charge separation[69]. After 6 h of visible light irradiation, the average rate of CO evolution was 24.8 μmol·g^{-1}·h^{-1} for Cu_6-NH [Figure 21H], comparable with reported catalysts[70-72]. Whereas Cu_6-N showed a low CO evolution rate of 4.3 μmol·g^{-1}·h^{-1}. Additionally, a minor amount of H_2 was detected, and O_2 was also generated with a molar ratio of 2:1 of CO and O_2. The sole difference between Cu_6-NH and Cu_6-N is the two protonated N atoms of the PymSH ligand in the former, as shown in Figure 21B, which play a key role as proton relay stations in improving its photocatalytic performance.

To gain further insights, *in situ* diffuse reflectance infrared Fourier transform spectroscopy (DRIFTS) experiments were conducted, revealing relatively extra absorption bands of *COOH, mCO_3^{2-}, and $b\text{-}CO_3^{2-}$ at 1,618, 1,517, and 1,342 cm^{-1}, respectively, for Cu_6-NH, ascribed to H-bonding between protonated N-H and different intermediates [Figure 21I and J]. This observation further validated the role of protonated N-H groups as proton relay stations in Cu_6-NH, beneficial for the formation of the *COOH intermediate, which was finally reduced to CO.

CO selective PCO_2RR: effect of structural transformation

The efficiency of photocatalytic CO_2 reduction has still not reached its full potential due to inadequate utilization of the solar spectrum. Recently, Dong *et al.* presented an unprecedented near-infrared light-responsive $[Cu_8(S^tBu)_4(PymS)_4]$ (Cu_8SN) nanocluster for effective photoreduction of CO_2[73]. Notably, owing to C-H…π and C-H…N interactions between PymS and ^{t}BuS-ligands shown in Figure 22A, a 3D supramolecular network is formed in Cu_8SN [Figure 22B]. Further, thermal treatment of Cu_8SN at 240 °C under N_2 resulted in its transformation into a novel and structurally stable $[Cu_8(S)_2(PymS)_4]$ (Cu_8SN-T) nanocluster [Figure 22C]. Comparison of the structures of Cu_8SN and Cu_8SN-T revealed that after heat treatment at 240 °C, the tert-butyl mercaptan uniting two Cu_4 sub-cores in Cu_8SN is replaced with S^{2-} in Cu_8SN-T, resulting in a novel Cu_8 Core in the latter [Figure 22A and C].

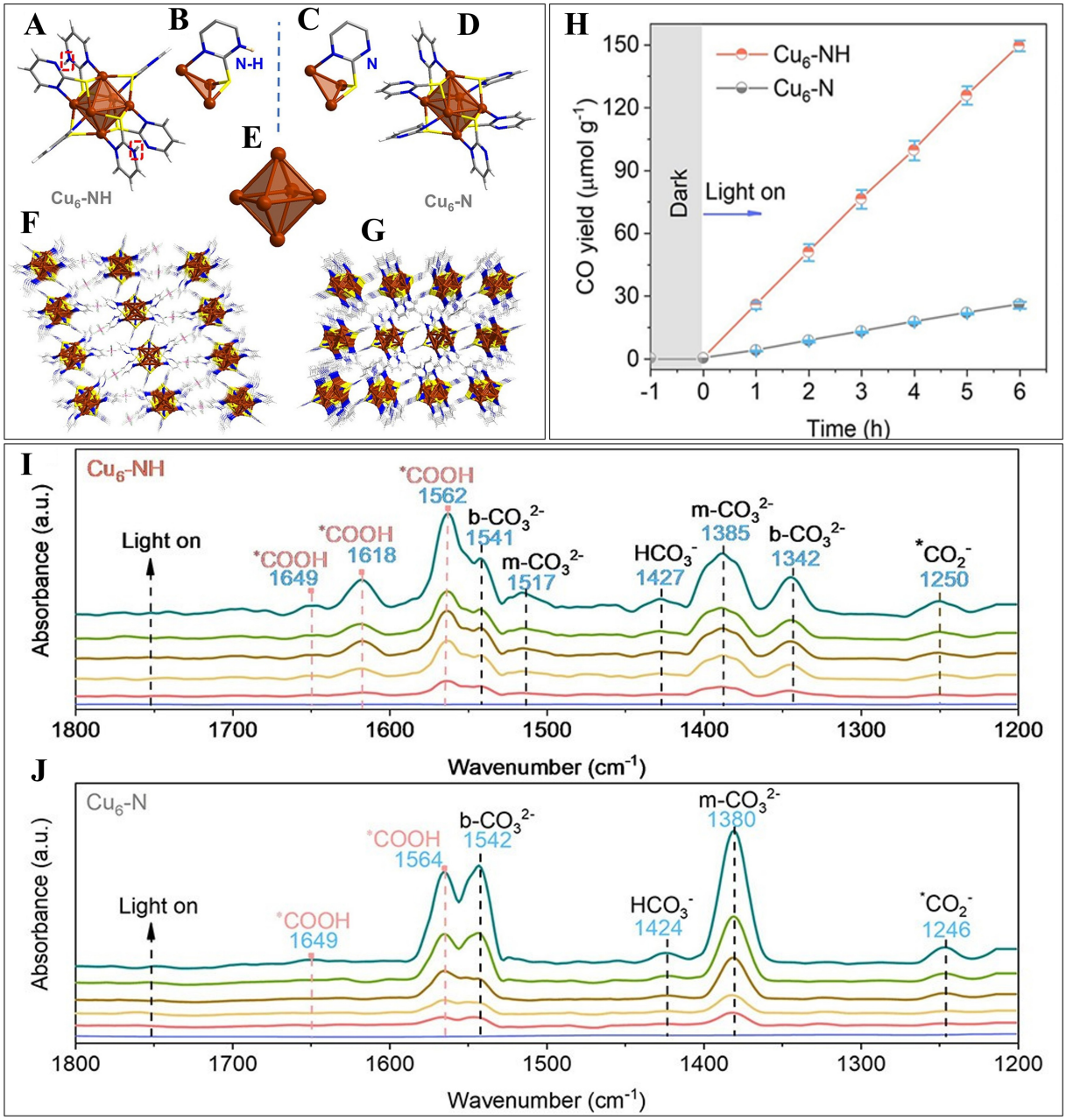

Figure 21. (A) Structure of Cu_6-NH ; (B) Coordination modes of ligand in Cu_6-NH ; (C) Coordination modes of ligand in Cu_6-N; (D) Structure of Cu_6-N; (E) Common octahedral Cu_6 metal core in Cu_6-NH and Cu_6-N; Molecule packing diagrams of (F) Cu_6-NH and (G) Cu_6-N; (H) Time-dependent CO_2 photoreduction performances of Cu_6-NH and Cu_6-N; In-situ DRIFTS spectra during CO_2 photoreduction over (I) Cu_6-NH and (J) Cu_6-N. Color code: Cu, brown; S, yellow; C, gray; H, white; N, blue. This figure is reproduced with permission from Ref.[69], © 2023 Wiley-VCH GmbH.

The estimated band gaps of 2.45 eV and 1.58 eV from Tauc plots for Cu_8SN and Cu_8SN-T, respectively [Figure 22D], confirmed their different band structures. Ultraviolet-visible-near infrared (UV-Vis-NIR) diffuse reflectance spectra (DRS) in Figure 22E revealed that Cu_8SN-T exhibited absorption bands across the UV-Vis-NIR region. Upon illumination with near-infrared (NIR) light (808 nm, 100 mW·cm^{-2}) [Figure 22F], the temperature of Cu_8SN-T increased from 24.2 to 87.2 °C within 25 s, which is much faster than for Cu_8SN (final temperature = 31.3 °C). Thus, Cu_8SN-T enables direct use of sunlight for high-temperature photocatalysis. Being a direct band gap semiconductor, the valence band of Cu_8SN-T at +0.90 V [*vs.* normal

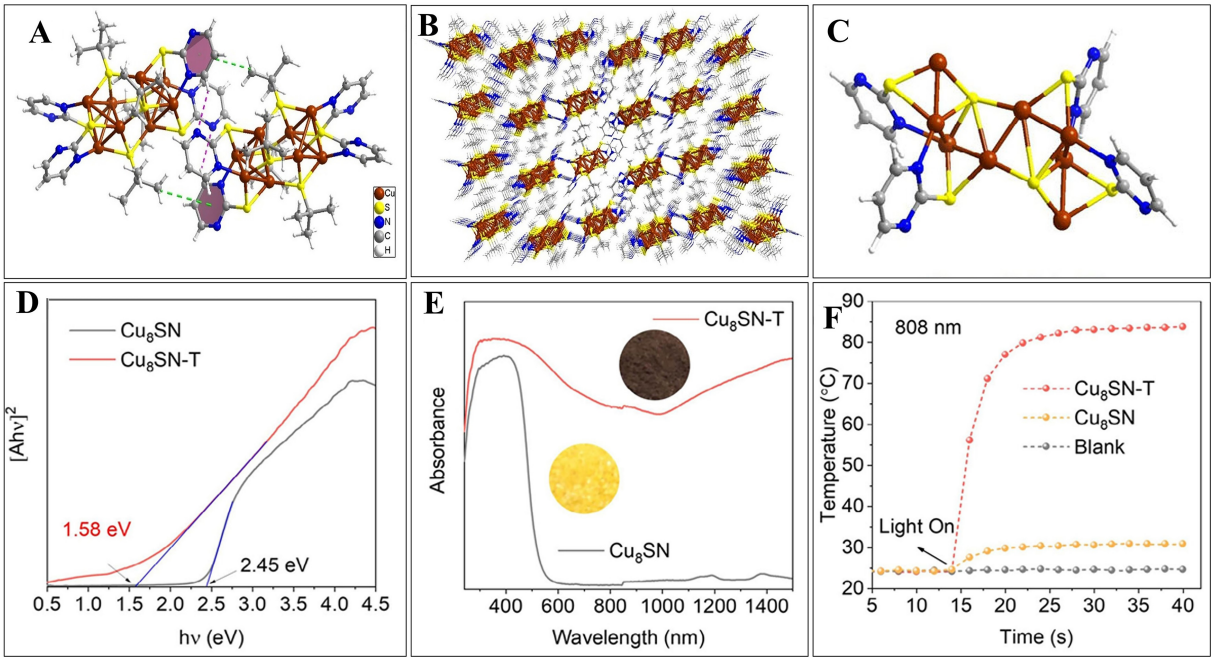

Figure 22. (A) C-H---π and C-H---N interactions in Cu_8SN; (B) Stacking structure of Cu_8SN; (C) Simulated structure of Cu_8SN-T; (D) Tauc plots of Cu_8SN and Cu_8SN-T showing their distinct band gaps; (E) Solid-state UV-Vis-NIR DRS of Cu_8SN and Cu_8SN-T (F) Photothermal temperature study of Cu_8SN and Cu_8SN-T. This figure is reproduced with permission from Ref.[73], © 2025 Wiley-VCH GmbH.

hydrogen electrode (NHE)] and the conduction band at -0.68 V (*vs.* NHE) make it possible to catalyze both CO_2 reduction and H_2O oxidation. Further, the quenching of PL intensity of Cu_8SN-T also confirmed its better charge separation ability.

The CO evolution rate of Cu_8SN-T was calculated to be 20.2, 17.92, and 7.1 μmol·g^{-1}·h^{-1} under full-spectrum light, Vis-NIR light, and NIR light, respectively, as presented in Figure 23A, which was higher than that of commercially available Cu_2S[73]. In contrast, the CO evolution rate of Cu_8SN was 3.1 and 2.6 μmol·g^{-1}·h^{-1} under full-spectrum light and Vis-NIR light, respectively, which decreased with time, whereas no products were formed under NIR light[73]. Thus, ligand removal improved the photocatalytic performance of CO evolution of Cu_8SN-T. Notably, the O_2 generation rate was nearly half that of CO evolution in these photocatalytic measurements.

In situ DRIFTS spectra shown in Figure 23B and C revealed that apart from the peaks owing to CO_2 adsorption on Cu_8SN-T at 2,335 and 2,360 cm^{-1}, additional peaks at 1,397, 1,558, and 1,649 cm^{-1} were assigned to the *COOH intermediate responsible for CO_2 reduction to CO. The bands at 1,432 and 1,742 cm^{-1} correspond to symmetric stretching of $*HCO_3^-$, highlighting that CO_2 and H_2O are co-adsorbed on Cu_8SN-T.

DFT calculations identified three types of Cu sites for CO_2 adsorption in Cu_8SN-T as shown in the inset of Figure 23D: A site (Cu-S_2), B site (Cu-N_1S_2), and C site (Cu-S_3) with adsorption energies of -0.31, -0.60, and -0.99 eV, respectively, indicating that any of them can act as a site for CO_2 reduction. However, CO_2 reduction was found more likely to occur at the C site (i.e., Cu-S_3) in the thermally treated Cu_8SN-T cluster as per their energy profiles [Figure 23D]. On the basis of DRIFTS results, authors proposed a plausible reaction mechanism of PCO_2RR over Cu_8SN-T shown in Figure 23E.

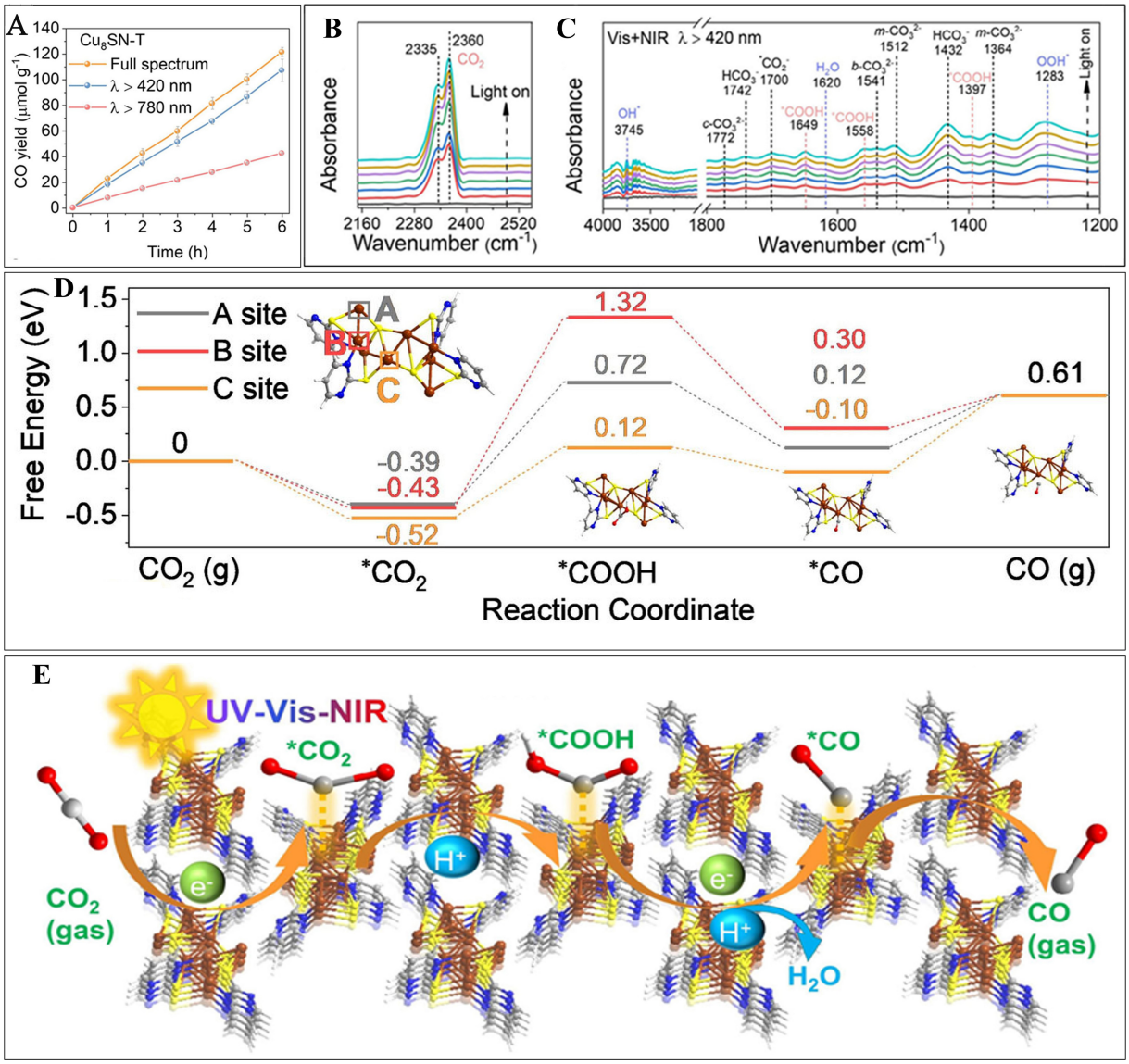

Figure 23. (A) CO_2RR performance of Cu_8SN-T; (B and C) *In situ* DRIFTS spectra during CO_2 photoreduction over Cu_8SN-T; (D) Free-energy diagrams for CO_2 reduction over A, B, and C sites of Cu_8SN-T; (E) CO_2RR mechanism. The asterisk (*) is standard notation for adsorbed species. This figure is reproduced with permission from Ref.[73], © 2025 Wiley-VCH GmbH. DRIFTS: Diffuse reflectance infrared Fourier transform spectroscopy.

CONCLUSIONS AND OUTLOOKS

In summary, the reported examples of electrochemical and photochemical reduction of CO_2 catalyzed by ligand-protected Cu metal nanoclusters with well-resolved structures are thoroughly reviewed in this article. Owing to the specific and well-defined catalytic active sites on the surface/interface of Cu metal nanoclusters and the optimal interaction of Cu with CO_2, deep mechanistic insights into ECO_2RR/PCO_2RR for the selective valuable products have been gained.

However, the following gaps need to be addressed. (a) The progress in the synthesis of Cu nanoclusters with well-resolved structures has not yet reached the level vis-à-vis their Au/Ag counterparts. The unexplored composition of Cu nanoclusters, particularly with partial Cu(0) character and even higher magic number clusters of Cu, are still to be discovered; (b) The stability of Cu nanoclusters is another area of concern for their applications in ECO_2RR/PCO_2RR that is required to be addressed; (c) Given the limited number of

reports, the photocatalytic CO_2 reduction over Cu nanoclusters must be a major research priority; (d) Considering the challenges to stabilize the Cu nanoclusters, more advancement is required in resolving their crystal structures and tailored optimization using theoretical research tools to unleash their full potential in CO_2RR catalysis; (e) The competitive reactions, particularly HER, occurring during CO_2RR over Cu nanoclusters should be suppressed efficiently to enhance FE and current density of targeted value-added hydrocarbon products for the practical applications; (f) The challenges to develop the surface engineering methods to increase the performance of Cu-based nanoclusters towards CO_2RR while working with CO_2 feed streams containing impurities, particularly in the industrial steel plants, must be overcome.

DECLARATIONS

Acknowledgments

Sharma, S. acknowledges VIT-AP University, Andhra Pradesh, India, for RGEMS support for the work.

Authors' contributions

Proposed the topic: Sharma, S.
Wrote the original draft: Sharma, S.; Li, G.
Revised and corrected the manuscript: Guddati, V.; Arasala, N.

Availability of data and materials

Not applicable.

AI and AI-assisted tools statement

Not applicable.

Financial support and sponsorship

The financial support under the RGEMS project from VIT-AP University, Andhra Pradesh, India (Order no. VIT-AP/SpoRIC/RGEMS/2022-23(II)/014) is highly acknowledged by Sharma, S.

Conflicts of interest

All authors declared that there are no conflicts of interest.

Ethical approval and consent to participate

Not applicable.

Consent for publication

Not applicable.

REFERENCES

1. Yu, J.; Wang, J.; Ma, Y.; et al. Recent progresses in electrochemical carbon dioxide reduction on copper-based catalysts toward multicarbon products. *Adv. Funct. Mater.* **2021**, *31*, 2102151. DOI
2. Jin, R.; Li, G.; Sharma, S.; Li, Y.; Du, X. Toward active-site tailoring in heterogeneous catalysis by atomically precise metal nanoclusters with crystallographic structures. *Chem. Rev.* **2021**, *121*, 567-648. DOI PubMed
3. Wang, G.; Chen, J.; Ding, Y.; et al. Electrocatalysis for CO_2 conversion: from fundamentals to value-added products. *Chem. Soc. Rev.* **2021**, *50*, 4993-5061. DOI
4. Irie, T.; Sasaki, K.; Das, S.; Negishi, Y. Materials innovation and the changing face of photocatalytic and electrocatalytic carbon dioxide reduction research: from metal nanoclusters to extended frameworks. *Angew. Chem. Int. Ed. Engl.* **2025**, *64*, e202515667. DOI PubMed PMC
5. Huang, J.; Zhang, X.; Yang, J.; Yu, J.; Chen, Q.; Peng, L. Recent progress on copper-based bimetallic heterojunction catalysts for CO_2 electrocatalysis: unlocking the mystery of product selectivity. *Adv. Sci.* **2024**, *11*, e2309865. DOI PubMed PMC

6. Nitopi, S.; Bertheussen, E.; Scott, S. B.; et al. Progress and perspectives of electrochemical CO_2 reduction on copper in aqueous electrolyte. *Chem. Rev.* **2019**, *119*, 7610-72. DOI PubMed
7. Hori, Y.; Kikuchi, K.; Suzuki, S. Production of CO and CH_4 in electrochemical reduction of CO_2 at metal electrodes in aqueous hydrogen carbonate solution. *Chem. Lett.* **1985**, *14*, 1695-8. DOI
8. Hori, Y.; Kikuchi, K.; Murata, A.; Suzuki, S. Production of methane and ethylene in electrochemical reduction of carbon dioxide at copper electrode in aqueous hydrogencarbonate solution. *Chem. Lett.* **1986**, *15*, 897-8. DOI
9. Hori, Y.; Murata, A.; Takahashi, R.; Suzuki, S. Enhanced formation of ethylene and alcohols at ambient temperature and pressure in electrochemical reduction of carbon dioxide at a copper electrode. *J. Chem. Soc,. Chem. Commun.* **1988**, *24*, 17-9. DOI
10. Hori, Y.; Murata, A.; Takahashi, R. Formation of hydrocarbons in the electrochemical reduction of carbon dioxide at a copper electrode in aqueous solution. *J. Chem. Soc.,. Faraday. Trans. 1.* **1989**, *85*, 2309-26. DOI
11. Kuhl, K. P.; Cave, E. R.; Abram, D. N.; Jaramillo, T. F. New insights into the electrochemical reduction of carbon dioxide on metallic copper surfaces. *Energy. Environ. Sci.* **2012**, *5*, 7050-9. DOI
12. Kuhl, K. P.; Hatsukade, T.; Cave, E. R.; Abram, D. N.; Kibsgaard, J.; Jaramillo, T. F. Electrocatalytic conversion of carbon dioxide to methane and methanol on transition metal surfaces. *J. Am. Chem. Soc.* **2014**, *136*, 14107-13. DOI PubMed
13. Peterson, A. A.; Nørskov, J. K. Activity descriptors for CO_2 electroreduction to methane on transition-metal catalysts. *J. Phys. Chem. Lett.* **2012**, *3*, 251-8. DOI
14. Lee, H.; Park, N.; Kong, T. H.; et al. Advancements in electrochemical methanol synthesis from CO_2: mechanisms and catalyst developments. *Nano. Energy.* **2024**, *130*, 110099. DOI
15. Gu, Z.; Shen, H.; Shang, L.; Lv, X.; Qian, L.; Zheng, G. Nanostructured copper-based electrocatalysts for CO_2 reduction. *Small. Methods.* **2018**, *2*, 1800121. DOI
16. Wang, Y.; Liu, J.; Wang, Y.; Al-Enizi, A. M.; Zheng, G. Tuning of CO_2 reduction selectivity on metal electrocatalysts. *Small* **2017**, *13*, 1701809. DOI PubMed
17. Zhao, J.; Xue, S.; Barber, J.; Zhou, Y.; Meng, J.; Ke, X. An overview of Cu-based heterogeneous electrocatalysts for CO_2 reduction. *J. Mater. Chem. A.* **2020**, *8*, 4700-34. DOI
18. Mrabet, A.; Merino-Garcia, I.; Perfecto-Irigaray, M.; Beobide, G.; Khaddor, M.; Albo, J. Green copper oxide photocathodes using plant extracts for an efficient photoelectrochemical CO_2 conversion to alcohols. *J. CO_2. Util.* **2025**, *101*, 103222. DOI
19. Du, Y.; Sheng, H.; Astruc, D.; Zhu, M. Atomically precise noble metal nanoclusters as efficient catalysts: a bridge between structure and properties. *Chem. Rev.* **2020**, *120*, 526-622. DOI PubMed
20. Kawawaki, T.; Okada, T.; Hirayama, D.; Negishi, Y. Atomically precise metal nanoclusters as catalysts for electrocatalytic CO_2 reduction. *Green. Chem.* **2024**, *26*, 122-63. DOI
21. Ghosh, M.; Sarma, R.; Kamiyama, M.; Kawawaki, T.; Biswas, S.; Negishi, Y. Next-generation CO_2 electroreduction: the role of atomically precise nanoclusters and emerging catalytic strategies. *Nanoscale. Horiz.* **2025**, *10*, 1250-67. DOI
22. Dinh, K. H.; Menisa, L. T.; Warkentin, H.; Nguyen, T. N.; Dinh, C. T. Metal cluster catalysts for electrochemical CO_2 reduction. *ACS. Catal.* **2025**, *15*, 5731-59. DOI
23. Baghdasaryan, A.; Bürgi, T. Copper nanoclusters: designed synthesis, structural diversity, and multiplatform applications. *Nanoscale* **2021**, *13*, 6283-340. DOI PubMed
24. Kawawaki, T.; Okada, T.; Takemae, K.; Tomihari, S.; Negishi, Y. Size-dependent carbon dioxide reduction activity of copper nanoparticle and nanocluster electrocatalysts. *ChemNanoMat* **2024**, *10*, e202300575. DOI
25. Li, S.; Nagarajan, A. V.; Li, Y.; Kauffman, D. R.; Mpourmpakis, G.; Jin, R. The role of ligands in atomically precise nanocluster-catalyzed CO_2 electrochemical reduction. *Nanoscale* **2021**, *13*, 2333-7. DOI
26. Kauffman, D. R.; Alfonso, D.; Matranga, C.; Qian, H.; Jin, R. Experimental and computational investigation of Au_{25} clusters and CO_2: a unique interaction and enhanced electrocatalytic activity. *J. Am. Chem. Soc.* **2012**, *134*, 10237-43. DOI PubMed
27. Kauffman, D. R.; Thakkar, J.; Siva, R.; et al. Efficient electrochemical CO_2 conversion powered by renewable energy. *ACS. Appl. Mater. Interfaces.* **2015**, *7*, 15626-32. DOI PubMed
28. Biswas, S.; Negishi, Y. Exploring the impact of various reducing agents on Cu nanocluster synthesis. *Dalton. Trans.* **2024**, *53*, 9657-63. DOI PubMed
29. Dhayal, R. S.; van Zyl, W. E.; Liu, C. W. Polyhydrido copper clusters: synthetic advances, structural diversity, and nanocluster-to-nanoparticle conversion. *Acc. Chem. Res.* **2016**, *49*, 86-95. DOI PubMed
30. Nematulloev, S.; Huang, R. W.; Yin, J.; et al. $[Cu_{15}(PPh_3)_6(PET)_{13}]^{2+}$: a copper nanocluster with crystallization enhanced photoluminescence. *Small* **2021**, *17*, e2006839. DOI PubMed

31. Li, H.; Zhai, H.; Zhou, C.; et al. Atomically precise copper cluster with intensely near-infrared luminescence and its mechanism. *J. Phys. Chem. Lett.* **2020**, *11*, 4891-6. DOI PubMed
32. Ke, F.; Song, Y.; Li, H.; Zhou, C.; Du, Y.; Zhu, M. Sub-nanometer Cu(i) clusters: coordination-modulated (Se *vs*. S) atom-packing mode and emission. *Dalton. Trans.* **2019**, *48*, 13921-4. DOI PubMed
33. Tang, J.; Liu, C.; Zhu, C.; et al. High-nuclearity and thiol protected core-shell $[Cu_{75}(S\text{-}Adm)_{32}]^{2+}$: distorted octahedra fixed to Cu_{15} core via strong cuprophilic interactions. *Nanoscale* **2023**, *15*, 2843-8. DOI PubMed
34. Wang, L.; Yan, X.; Tian, G.; et al. Chiral copper-hydride nanoclusters: synthesis, structure, and assembly. *Dalton. Trans.* **2023**, *52*, 3371-7. DOI PubMed
35. Dong, G.; Pan, Z.; Han, B.; et al. Multi-layer 3D Chirality and Double-Helical Assembly in a Copper Nanocluster with a Triple-Helical Cu_{15}Core. *Angew. Chem. Int. Ed. Engl.* **2023**, *62*, e202302595. DOI
36. Sun, C.; Mammen, N.; Kaappa, S.; et al. Atomically precise, thiolated copper-hydride nanoclusters as single-site hydrogenation catalysts for ketones in mild conditions. *ACS. Nano.* **2019**, *13*, 5975-86. DOI PubMed PMC
37. Han, B. L.; Liu, Z.; Feng, L.; et al. Polymorphism in Atomically Precise Cu_{23} nanocluster incorporating tetrahedral $[Cu_4]^0$ kernel. *J. Am. Chem. Soc.* **2020**, *142*, 5834-41. DOI PubMed
38. Nguyen, T. A. D.; Jones, Z. R.; Goldsmith, B. R.; et al. A Cu_{25} nanocluster with partial Cu(0) character. *J. Am. Chem. Soc.* **2015**, *137*, 13319-24. DOI PubMed
39. Das, A. K.; Biswas, S.; Wani, V. S.; Nair, A. S.; Pathak, B.; Mandal, S. $[Cu_{18}H_3(S\text{-}Adm)_{12}(PPh_3)_4Cl_2]$: fusion of Platonic and Johnson solids through a Cu(0) center and its photophysical properties. *Chem. Sci.* **2022**, *13*, 7616-25. DOI PubMed PMC
40. Li, Y. L.; Wang, J.; Luo, P.; et al. Cu_{14} Cluster with Partial Cu(0) character: difference in electronic structure from isostructural silver analog. *Adv. Sci.* **2019**, *6*, 1900833. DOI PubMed PMC
41. Jia, T.; Guan, Z. J.; Zhang, C.; et al. Eight-electron superatomic Cu_{31} nanocluster with chiral kernel and NIR-II emission. *J. Am. Chem. Soc.* **2023**, *145*, 10355-63. DOI PubMed
42. Gao, P.; Du, J.; Hong, W.; et al. Observation of Body-Centered-Cubic Cu nanocluster with partial Cu(0) character. *Small. Struct.* **2025**, *6*, 2400397. DOI
43. Biswas, S.; Shingyouchi, Y.; Kamiyama, M.; et al. Atomically precise $[Cu_{23}H_4(SC_7H_7)_{18}(PPh_3)_6]$ nanocluster: structural integration of johnson solids through a Cu(0) center and electrocatalytic functionality. *J. Am. Chem. Soc.* **2025**, *147*, 23733-42. DOI
44. Zhang, L. P.; Fang, J. J.; Liu, Z.; Xie, Y. P.; Lu, X. Recent progress in atomically precise Cu-M alloy nanoclusters. *Chem. Eur. J.* **2025**, *31*, e202404281. DOI
45. Deng, G.; Kim, J.; Bootharaju, M. S.; et al. Body-centered-cubic-kernelled $Ag_{15}Cu_6$ nanocluster with alkynyl protection: synthesis, total structure, and CO_2 electroreduction. *J. Am. Chem. Soc.* **2023**, *145*, 3401-7. DOI PubMed
46. Chen, X. Y.; Li, L. Y.; Zhao, L. C.; et al. Ag^+-Mediated structural reconstruction of a metastable Cu_{35} cluster toward Cu-Ag heterometallic architectures for superior electrocatalytic CO_2-to-ethanol conversion. *Angew. Chem. Int. Ed. Engl.* **2025**, *64*, e202511232. DOI PubMed
47. Lee, S.; Bootharaju, M. S.; Deng, G.; et al. $[Pt_2Cu_{34}(PET)_{22}Cl_4]^{2-}$: An atomically precise, 10-electron PtCu bimetal nanocluster with a direct Pt–Pt bond. *J. Am. Chem. Soc.* **2021**, *143*, 12100-7. DOI PubMed
48. Peng, S. K.; Yang, H.; Luo, D.; Ning, G. H.; Li, D. A highly NIR emissive $Cu_{16}Pd_1$ nanocluster. *Small* **2024**, *20*, e2306863. DOI PubMed
49. Zhang, X.; Guo, S. X.; Gandionco, K. A.; Bond, A. M.; Zhang, J. Electrocatalytic carbon dioxide reduction: from fundamental principles to catalyst design. *Mater. Today. Adv.* **2020**, *7*, 100074. DOI
50. Zhang, Y.; Guo, S.; Zhang, X.; Bond, A. M.; Zhang, J. Mechanistic understanding of the electrocatalytic CO_2 reduction reaction - new developments based on advanced instrumental techniques. *Nano. Today.* **2020**, *31*, 100835. DOI
51. Sun, Z.; Ma, T.; Tao, H.; Fan, Q.; Han, B. Fundamentals and challenges of electrochemical CO_2 reduction using two-dimensional materials. *Chem* **2017**, *3*, 560-87. DOI
52. Sikdar, N. Electrochemical CO_2 reduction reaction: comprehensive strategic approaches to catalyst design for selective liquid products formation. *Chemistry* **2024**, *30*, e202402477. DOI PubMed
53. Chang, B.; Pang, H.; Raziq, F.; et al. Electrochemical reduction of carbon dioxide to multicarbon (C_{2+}) products: challenges and perspectives. *Energy. Environ. Sci.* **2023**, *16*, 4714-58. DOI
54. Tang, Q.; Lee, Y.; Li, D. Y; et al. Lattice-hydride mechanism in electrocatalytic CO_2 reduction by structurally precise copper-hydride nanoclusters. *J. Am. Chem. Soc.* **2017**, *139*, 9728-36. DOI
55. Shingyouchi, Y.; Ogami, M.; Biswas, S.; et al. Ligand-dependent intracluster interactions in electrochemical CO_2 reduction using Cu_{14} nanoclusters. *Small* **2025**, *21*, e2409910. DOI PubMed PMC

56. Liu, L. J.; Wang, Z. Y.; Wang, Z. Y.; Wang, R.; Zang, S. Q.; Mak, T. C. W. Mediating CO_2 electroreduction activity and selectivity over atomically precise copper clusters. *Angew. Chem. Int. Ed. Engl.* **2022**, *61*, e202205626. DOI PubMed
57. Han, B. L.; Zhao, L. C.; Yuan, Z. R.; et al. Dipropyne-modified N-heterocyclic carbene stabilized atomically precise copper(I) nanocluster catalysts for CO_2 electroreduction. *Adv. Funct. Mater.* **2025**, *35*, 2500149. DOI
58. Wu, Q. J.; Si, D. H.; Sun, P. P.; et al. Atomically precise copper nanoclusters for highly efficient electroreduction of CO_2 towards hydrocarbons via breaking the coordination symmetry of cu site. *Angew. Chem. Int. Ed. Engl.* **2023**, *62*, e202306822. DOI PubMed
59. Biswas, S.; Tanaka, T.; Song, H.; et al. Highly selective methanol synthesis using electrochemical CO_2 reduction with defect-engineered Cu_{58} nanoclusters. *Small. Sci.* **2024**, *5*, 2400465. DOI PubMed PMC
60. Biswas, S.; Hossian, S.; Kosaka, T.; et al. Nested Keplerian architecture of $[Cu_{58}H_{20}(SPr)_{36}(PPh_3)_8]^{2+}$nanoclusters. *Chem. Commun.* **2023**, *59*, 9336-9. DOI PubMed
61. Li, S.; Yan, X.; Tang, J.; et al. Cu_{26} nanoclusters with quintuple ligand shells for CO_2 electrocatalytic reduction. *Chem. Mater.* **2023**, *35*, 6123-32. DOI
62. Chen, A.; Kang, X.; Jin, S.; Du, W.; Wang, S.; Zhu, M. Gram-scale preparation of stable hydride M@Cu_{24} (M = Au/Cu) nanoclusters. *J. Phys. Chem. Lett.* **2019**, *10*, 6124-8. DOI PubMed
63. Yuan, P.; Chen, R.; Zhang, X.; et al. Ether-Soluble Cu_{53} nanoclusters as an effective precursor of high-quality CuI films for optoelectronic applications. *Angew. Chem. Int. Ed. Engl.* **2019**, *58*, 835-9. DOI PubMed
64. Ghosh, A.; Huang, R. W.; Alamer, B.; et al. $[Cu_{61}(S^tBu)_{26}S_6Cl_6H_{14}]^+$: a core-shell superatom nanocluster with a Quasi-J_{36} Cu_{19} core and an "18-Crown-6" metal-sulfide-like stabilizing belt. *ACS. Materials. Lett.* **2019**, *1*, 297-302. DOI
65. Xie, Y.; Liu, L. J.; Lu, Q.; Wu, W.; He, J.; Wang, Y. Tuning Cu nanocluster size for methane production in a bipolar membrane CO_2 electrolyzer. *Energy. Fuels.* **2025**, *39*, 17661-8. DOI
66. Han, C.; Yang, T.; Fang, Y.; et al. Steering the product selectivity of CO_2 electroreduction by single atom switching in isostructural copper nanocluster catalysts. *Angew. Chem. Int. Ed. Engl.* **2025**, *64*, e202503417. DOI PubMed
67. Li, J. K.; Dong, J. P.; Liu, S. S.; et al. Promoting CO_2 electroreduction to hydrocarbon products via sulfur-enhanced proton feeding in atomically precise thiolate-protected Cu clusters. *Angew. Chem. Int. Ed. Engl.* **2024**, *63*, e202412144. DOI PubMed
68. Handoko, A. D.; Li, K.; Tang, J. Recent progress in artificial photosynthesis: CO_2 photoreduction to valuable chemicals in a heterogeneous system. *Curr. Opin. Chem. Eng.* **2013**, *2*, 200-6. DOI
69. Dong, J. P.; Xu, Y.; Zhang, X. G.; et al. Copper-sulfur-nitrogen cluster providing a local proton for efficient carbon dioxide photoreduction. *Angew. Chem. Int. Ed. Engl.* **2023**, *62*, e202313648. DOI PubMed
70. Wang, Y.; Qu, Y.; Qu, B.; et al. Construction of six-oxygen-coordinated single Ni sites on g-C_3N_4 with boron-oxo species for photocatalytic water-activation-induced CO_2 reduction. *Adv. Mater.* **2021**, *33*, 2105482. DOI PubMed
71. Wang, S.; Xu, M.; Peng, T.; et al. Porous hypercrosslinked polymer-TiO2-graphene composite photocatalysts for visible-light-driven CO2 conversion. *Nat. Commun.* **2019**, *10*, 676. DOI PubMed PMC
72. Lu, M.; Zhang, M.; Liu, J.; et al. Confining and highly dispersing single polyoxometalate clusters in covalent organic frameworks by covalent linkages for CO_2 photoreduction. *J. Am. Chem. Soc.* **2022**, *144*, 1861-71. DOI PubMed
73. Dong, J. P.; Li, J. K.; Zhang, H.; et al. Accurate thermal resection of atomically precise copper clusters to achieve near-IR light-driven CO_2 reduction. *Adv. Mater.* **2025**, *37*, e2417747. DOI PubMed